Study on The Effect of Production Dynamic to Fault Reactivation

A Case Study of Groningen Gas Field

Ghina K. Ihsan

4521900

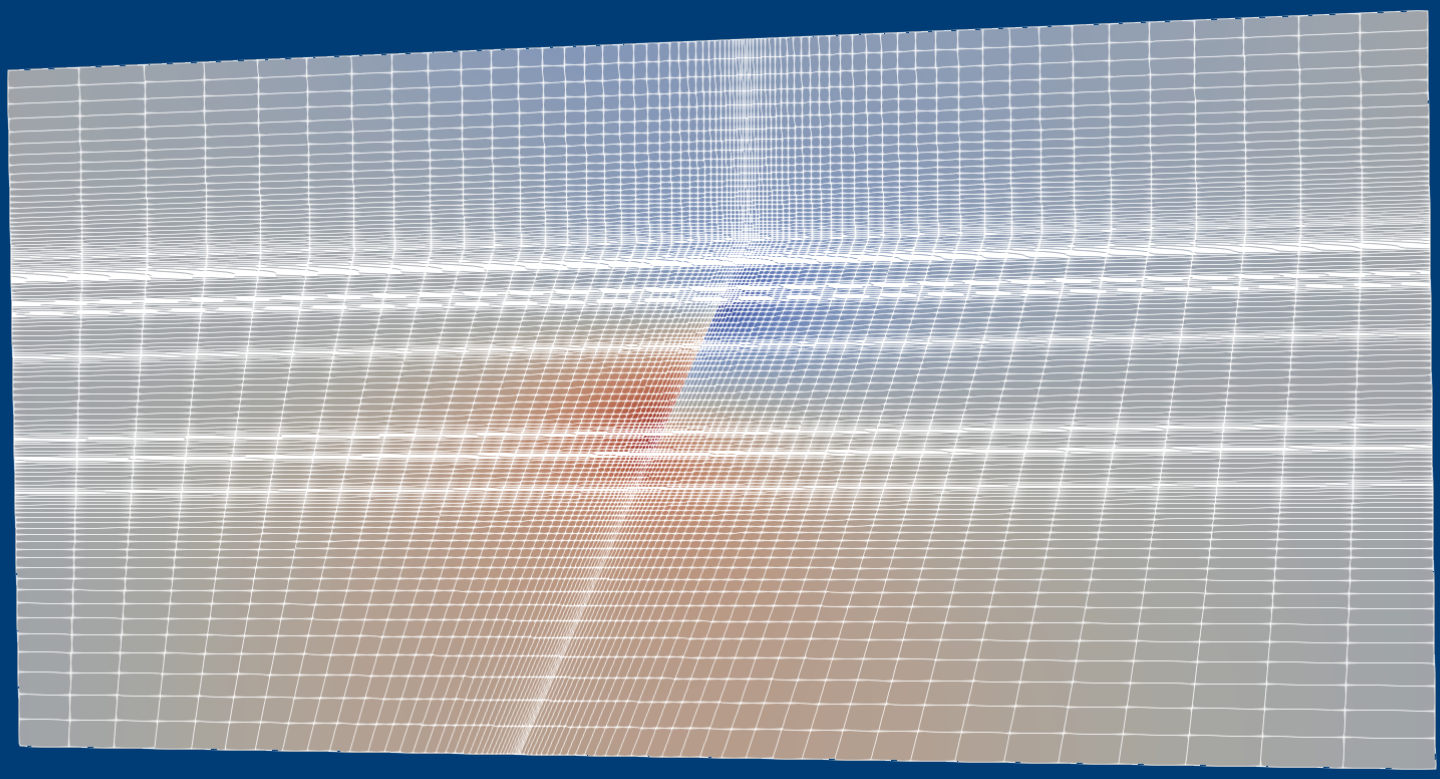

TU Delft

Study on The Effect of Production Dynamic to Fault Reactivation

A Case Study of Groningen Gas Field

by

Ghina K. Ihsan

A thesis submitted to the department of Petroleum Engineering at
the Technische Universiteit Delft in partial fulfillment of the requirements for the degree of
Master of Science

to be defended publicly on Thursday, 29 March 2018 at 11:00 AM.

Student number: 4521900

Thesis committee:		
	Dr. Denis Voskov,	TU Delft, supervisor
	Prof. Dr. Ir. Jan Dirk Jansen,	TU Delft
	Prof. Dr. Giovanni Bertotti,	TU Delft
	Dr. Ir. Femke Vossepoel,	TU Delft

Abstract

The subsurface of Groningen gas field composed of several faults. The continuous production has been resulting in several micro-seismicity activities, particularly for the past decades. One of the reasons for the production-induced-seismicity is fault reactivation at depth. The fault that initially in the non-active state becomes active and starts slipping due to pore fluid extraction. The modelling of fault reactivation induced by production can be simulated by coupling of flow and geomechanics.

The project studies the coupling of flow and geomechanics for an idealistic subsurface model with fault. The flow occurs due to pore pressure depletion and is predicted by solving mass conservation. The corresponding deformation is estimated by momentum balance equation.The observation will be limited to rock deformation that is quantified by effective stress and displacement on the fault due to a pressure change in the subsurface. The simulation is performed using Stanford's Automatic Differentiation General Purpose Reservoir Simulator (ADGPRS). In the proposed model, the flow equation is discretised using finite volume method, and poromechanics is discretised by finite-element Galerkin's approach. Both problems share the same grid model, and there is no error associated with the information exchange. The coupled problem is being solved fully implicitly where flow and mechanics formulation are solved simultaneously.

The case study for the simulation is a simplified Groningen subsurface model with a fault zone. The impact of variability in production dynamic on fault reactivation is studied. The variations in production rate and production strategy are applied in different formation configurations. It is found that the correlation between the production rates and the stress state in the subsurface depends on the formation offset. However, the stress field does not depend on continuity of the production scheme. Several aspects including the presence of Gas-Water contact in the model was studied in this project as well.

Keywords: Fault reactivation, gas depletion, ADGPRS, reservoir simulation, coupled of flow and geomechanics

Preface

I would like to thank Dr. Denis Voskov. I could learn a lot from him and I will always appreciate the energy and the commitment he had for the project. Thanks for always pushing us and for his high expectations that makes us reach great results.

Thanks to Dr. Timur Garipov from Stanford University, for his help, firstly in the construction of the geomechanical model and for all the time invested in fruitful discussions about my project.

Thanks to my friends: Reiner, Andrea, Kajeng for all the support and nice times we have created together during my time in this Master. Thank you Mutiara and Ariel who are constantly checking up on me. Also for the ones not mentioned, here and back home for being somehow always present.

Lastly my parents and the rest of my family for the encouragement and endless support in this period.

Ghina K. Ihsan
Delft, March 2018

Contents

List of Figures

List of Tables

1. Introduction

Hydrocarbons or other fluids in the subsurface are stored in the porous part of rocks. In the process of production, the pore fluid is extracted from the rock, thus the pore pressure decreases. As consequences, the overburden state would change as the formation depleted, so does its effective stress. Subsurface formations get compacted since the mechanical load increases. The reservoirs with a pre-existing fault become prone to slipping when the mechanical loads grow. Consequently, seismic activities could take place during compaction and when abrupt slip occurs on such faults. This phenomena can be studied by coupling of flow and geomechanics.

The recurring earthquakes in Groningen urged the NAM to make regulations about the gas production. Some of the regulations were to decrease the production rate and to delay production of shut-in the well for some days then reopen the well to continue production. These regulations are expected to make the earthquake occurring to be less frequent and the stress state in the subsurface to be more stable. This project will study how the production dynamics impact the fault reactivation which potentially induces seismicity.

1.1. State of the Art

Coupling of flow and geomechanics has been widely applied in developing hydrocarbon field which describes the interactions between fluid flow and mechanics. For instance, the coupling of hydraulic fracturing of shale gas reservoir is performed by injecting a large quantity of fluid to stimulate the flow [9]. Another example is CO_2 sequestration in the subsurface which over-pressurizes the formation and potentially induced seismicity and shear-slip on pre-existing faults [10]. In general, fluid injection and production at depth can be associated with subsidence and fault reactivation that result in the micro-seismic event. Several studies in predicting production induced seismicity due to fluid extraction (production) in the Groningen gas field had been carried out [7, 8, 11]. Moreover, details on the effect of pressure transients around the well bore to induced earthquake was also studied [12].

The earliest study regarding coupled phenomena which considered pore fluid flow and mechanics (quasi-static soil deformation) was developed by Terzaghi in 1923 who proposed a one-dimensional consolidation theory for saturated porous, permeable soils undergoing a constant loading [13, 14]. Biot [15] developed a settlement of linear poroelasticity theory. Rice and Cleary [16] remodelled Biot's constitutive equation and formulated fault propagation of fracture mechanics model, a phenomenon involving coupled behaviour between the rupturing solid and its pore fluid. The flow behaviour can be estimated using mass conservation, and the geomechanics response is approximated by momentum balance equation. The solutions of governing equations of coupled flow and geomechanics are normally addressed by numerical strategies. There has been several research that solved the problem with different approaches and assumptions. A sequential scheme for fractured reservoir and fault slip were respectively developed by [17] and [2]. In this project, the fully implicit formulation will be used to solve the nonlinear governing equations, the related constitutive relations and boundary conditions. The fully implicit method will simulate the problem simultaneously using ADGPRS [6, 18].

1.1.1. ADGPRS

Automatic Differentiation General Purpose Reservoir simulator (ADGPRS), is a simulator that was developed in SUPRI-B department at Stanford University. It is capable of handling multi-physics problem with several solution strategies. ADGPRS is a modular simulator that consists several physics modules, that are; compositional, thermal (heat), mechanics, reactions, wells and surface facilities. It can simulate flow and transport that entails physics processes by coupling strategies of one with another physics modules. The coupled problem can be solved with different strategies; sequential, fully implicit and implicit-sequential. The technique adopted to simulate flow in faulty media is the discrete fracture and matrix (DFM) model. A modified DFM model from Karimi-Fard work [5] will be used and approximated using finite volume method. Geomechanics equation will be discretised and approximated using finite element method [3].

1.2. Groningen Gas Field

Groningen field is the largest gas producing field in Western Europe that is located in the North-East of the Netherlands. The field was first discovered in 1959 and production has started since 1963 with gas reserves is around 2800 bcm. The geology of petroleum system is in the Carboniferous-Rotliegend, with source rock of Carboniferous Coal, a reservoir of Rotliegend sedimentary system and Zechstein evaporites as seal [19]. The gas accumulations in reservoir rocks are located in Slochteren formation from the Upper Rotliegend group, composed of Rotliegend Slochteren sandstone (ROSL) embedded with Ten Boer claystone (ROCLT). The top seal is a salt layer from Zechstein group (ZE). Both reservoir and cap rock were formed in the Permian age [20].

Table 1.1: Lithrostratigraphic subdivision of Groningen subsurface, adopted from [1]

Time	Group	Formation	Member	ReGeo Code
Permian	Zechstein			ZE
	Upper Rotliegend	Silverpit	Ten Boer Claystone	ROCLT
		Slochteren	Slochteren Sandstone	ROSL
Carboniferous	Limburg			DC

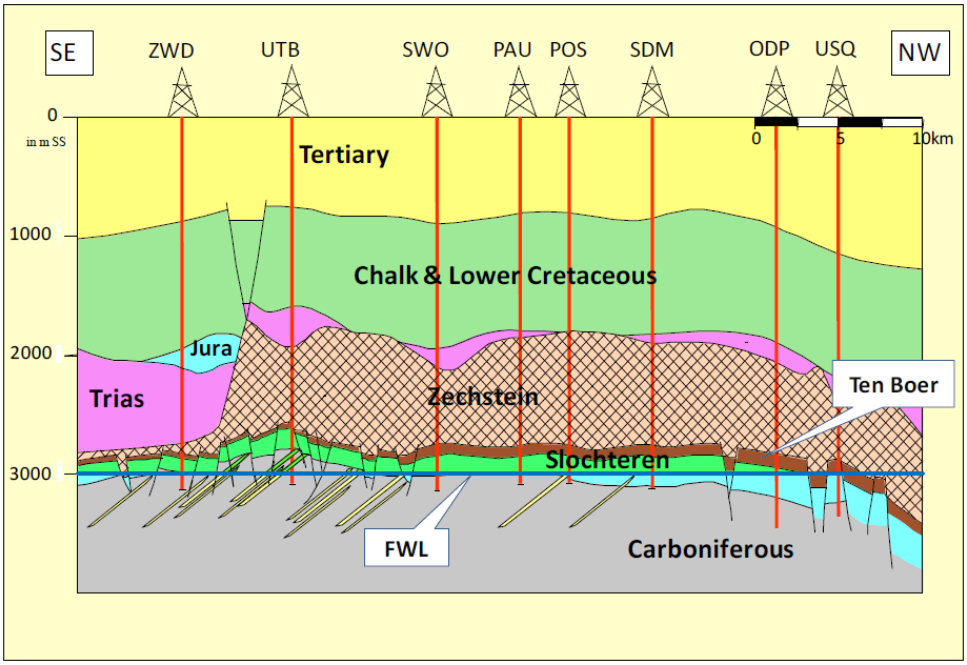

Figure 1.1: Geological illustration of Groningen field's subsurface ([1])

The geological structure of the field is located on Groningen High that dissected by a number of faults which some of these faults contribute to induced earthquakes. The faults were formed

due to extensional rifting process during Late Carboniferous / Early Permian and more developed until Saalian erosional event marking Carboniferous-Premian boundary. Most of these faults have been created by two major tectonic events. The first was extensional activities starting from the Triassic to the Late Jurassic and followed by an inversion stage during the late Jurassic-early Cretaceous (Kimmerian) resulting in Zechstein salt deposition in the late Cretaceous. Movement of Zechstein salt in Cretaceous time had added load to these faults. The second fault generation was due to compressional activities, and transpressions were formed correspondingly up to early Tertiary time[1, 19, 21]. Figure 1.1 illustrates the geological setting of Groningen field. FWL stands for free water level and located between Carboniferous to Slochteren formation.

1.3. Modeling

In 2015, Peter van den Bogert published a report about fault slip response from various modelling options [7]. The report assesses the impact of several parameters such as elastic parameters and model geometry on the fault behaviour during depletion processes. In our work, the model geometry and physical properties will be adapted from Bogert 2015 [7], that is the subsurface model of the Groningen gas field. The fault behaviour due to production will be evaluated with coupled of flow and geomechanics.

The fault surface is embedded explicitly in the model geometry, therefore, the unstructured grid will be used to discretise governing equations. The same grid will be used to approximate flow and geomechanics solutions so that the information exchange between the flow and geomechanics will be performed during simulation. For flow modelling, the fault is considered as heterogeneous permeability field whereas, in geomechanics, fault behaviour is perceived as a contact problem. The fault will be modelled as discontinuity surface using interface elements so that dynamics on the fault surface can be considered through stick-slip behaviour.

The model geometry consists of 4 layers; underburden layer at the bottom of the model, reservoir layer that consists of Slochteren sandstone and Ten Boer claystone, Zechstein salt layer as cap rock and overburden layer at the top. A fault intersects the two blocks; the hanging wall and the footwall block. The stress field undergoes a normal faulting regime.

The model grid is created using *gmsh* software with irregular quadrilateral mesh [22]. The physical properties are assigned using pre-processing code. The initiation of finite volume DFM and finite element, as well as initial and boundary conditions, are also being defined in the same code. The pre-processor generates this information as input files for ADGPRS. For the simulation in ADGPRS, an external linear solver library *Pardiso* is used with linearisation of the coupled flow and geo-mechanics problem based on the Newton-Raphson method. The ADGPRS output is visualized using *Paraview* [23] and *Matlab* [24].

The major assumptions for this modelling are that; the condition is isothermal, rock compressibility is constant, small deformation, and linear elasticity. The mathematical model of flow and geomechanics is explained in chapter 2.

1.4. Research Objectives

The main goal of this study is to perform the impact of various production strategies on fault reactivation using coupled fluid flow and geomechanics. The framework for this study is as follows:

- The initial work is to reproduce P.A.J van den Bogert work[7] that is fault behaviour due to depletion. The simulation will be performed to a different set of fault throw model; 0m, 80m, 215m and 440m of formation shift.
- Variations in production rate will also be simulated, and the result at the same pore volume produced will be compared.
- Different production strategy on fault reactivation for different reservoir configurations is also being modelled. Although sudden production change (open and shut-in of the well)

on the fault reactivation was studied [12], in this project the comparison of subsurface geomechanical state will be perform at the same cumulative gas produced.

1.5. Thesis Structure

Given the overview and framework of this thesis, the outline of this thesis report is as following:

- Chapter 1 introduces the overview of this study.
- Chapter 2 expresses the mathematical model and discretisation method.
- Chapter 3 describes the strategy and implementation of the numerical model.
- Chapter 4 represents the model validation.
- Chapter 5 is the sensitivity studies of the model.
- Chapter 6 is the example of a case study.
- Chapter 7 states the conclusions and recommendation.

2. Mathematical Model

The governing equations for flow and geomechanics is described in this chapter. To facilitate the mathematical model of coupled flow and geomechanics with a pre-existing fault present, the porous matrix and the fault will be treated as two different continua. The coupling between porous matrix and fault will be described in section 2.1 and 2.2. Governing equation for flow and geomechanics is obtained from the mass conservation and momentum balance, respectively [3].

2.1. Porous Matrix Dynamics

In this section, the governing equations describing flow and poroelastic response of reservoir matrix will be explained.

2.1.1. Single Phase Fluid Flow Equation

Governing equation is derived from the single-phase fluid mass balance equation. In this equation, fluid can only occupy porous media with a porosity of ϕ. If the fluid mass density is ρ_f, then the fluid mass of $\rho_f \phi \; d\Omega$ is contained in the material volume of $d\Omega$, therefore the macroscopic fluid mass density is $\rho_f \phi$. Fig.2.1 below depicts the conservation of mass inside a volume.

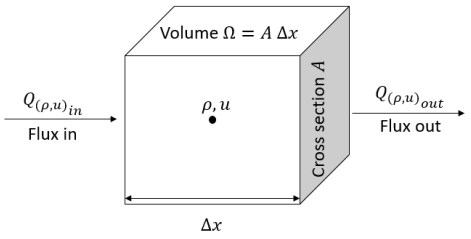

Figure 2.1: Conservation of mass for flow

The mass balance for the control volume is written as [25]:

$$\text{[rate of inflow]} - \text{[rate of outflow]} = \text{accumulation}$$

$$\begin{aligned} \int_{\partial\Omega} (\rho_f \phi \mathbf{v}) \cdot \mathbf{n} dA + \int_{\Omega} \frac{\partial}{\partial t}(\rho_f \phi) d\Omega = 0 \\ \int_{\Omega} \nabla \cdot (\rho_f \phi \mathbf{v}) d\Omega + \int_{\Omega} \frac{\partial}{\partial t}(\rho_f \phi) d\Omega = 0 \\ \int_{\Omega} \left[\nabla \cdot (\rho_f \phi \mathbf{v}) + \frac{\partial}{\partial t}(\rho_f \phi) \right] d\Omega = 0. \end{aligned} \tag{2.1}$$

The continuity equation is:

$$\frac{\partial \rho_f \phi}{\partial t} = -\nabla \cdot (\rho_f \phi \mathbf{u}), \tag{2.2}$$

where **u** denotes Darcy or superficial velocity that is derived from conservation of momentum.

The Darcy velocity is directly obtained by equating the pressure gradient with fluid and rock properties. Darcy flow equation can be expressed as [26]:

$$\mathbf{u} = -\frac{k}{\mu_f}\nabla(P + \rho_f \mathbf{g}), \tag{2.3}$$

where k denotes intrinsic skeleton permeability tensor, μ_f fluid viscosity, P pressure difference between two points and g gravity vector.

Combining the mass balance (eq.2.2) in which porosity is constant over space domain and Darcy equation (eq.2.3), the governing equation for flow is transformed to:

$$\frac{\partial(\rho_f \phi)}{\partial t} = \nabla \cdot \left[\rho_f \frac{k}{\mu_f}(\nabla p - \rho_f g)\right] + q \tag{2.4}$$

The first term is an accumulation term ($\frac{\partial(\rho_f \phi)}{\partial t}$) describing how fluid mass varies over time; the second term is fluid mass flux and q is the volumetric source term.

For compressible flow, fluid density is a function of pressure defined as:

$$\rho_f = \rho_{0,f} * (1 + c_f * (p - p_0)); \tag{2.5}$$

where $\rho_{0,f}$ is reference density at reference pressure p_0 and c_f is fluid compressibility.

2.1.2. Momentum Balance - Poroelasticity

In continuum mechanics, any material domain Ω is subjected to two external forces: body force **f** and surface force **T**. Body force occurs due to acceleration (e.g. gravity) and is defined as body force density per mass unit of the material ($\partial \mathbf{f} = \rho \mathbf{f}\, d\Omega$). Both of these forces depend on the vector position and time. Moreover, surface force **T** is directed based on outward unit normal **n** to dA. The latter force is called local contact force known as Cauchy's hypothesis on defining stress tensor [25].

Using classical continuum representation, the fluids and the matrix are considered as two overlapping continuum. The momentum balance within the porous domain is:

$$\begin{gathered} \frac{d^s}{dt}\int_\Omega \rho_s(1-\phi)\mathbf{v}^s\, d\Omega + \frac{d^f}{dt}\int_\Omega \rho_f \phi \mathbf{v}^f\, d\Omega = \int_\Omega \rho \mathbf{f}\, d\Omega + \int_{\partial\Omega} \mathbf{T}\, dA \\ \int_\Omega \left(\rho_s(1-\phi)\dot{\mathbf{v}}^s + \rho_f \phi \dot{\mathbf{v}}^f\right)\, d\Omega = \int_\Omega \rho \mathbf{f}\, d\Omega + \int_{\partial\Omega} \mathbf{T}\, dA \end{gathered} \tag{2.6}$$

where vector $\dot{\mathbf{v}}$ is acceleration (a time derivative of vector velocity **v**), and s and f are respectively solid (skeleton) and fluid particle. Material density ρ is defined as a bulk density including both skeleton and fluid:

$$\rho = \rho_s(1-\phi) + \rho_f \phi \tag{2.7}$$

When the surface force **T** is acting on small tetrahedron, that has three facets orientation $\mathbf{e}_j;\ j = 1;2;3$, combined with action reaction law, one can use tetrahedron lemma assuming tetrahedron height $h \to 0$. Applying tetrahedron lemma to the momentum balance (eq.2.6) results in a linear operator that links the vector **T** to normal vector n. Using Cauchy stress tensor, vector **T** can be called stress vector:

$$\mathbf{T} = \boldsymbol{\sigma} \cdot \mathbf{n} = \sigma_{ij} n_j \mathbf{e}_i \tag{2.8}$$

with stress tensor $\boldsymbol{\sigma}$ is consequence of local contact force of Cauchy's hypothesis, **T**.

Combining momentum balance (eq.2.6) with Cauchy stress tensor (eq.2.8) and using the di-

vergence theorem, the mass balance can be rewritten as:

$$\begin{aligned}\int_{\Omega}\left(\rho\mathbf{f}-\rho_s(1-\phi)\dot{\mathbf{v}}^s-\rho_f\phi\dot{\mathbf{v}}^f\right)\,d\Omega+\int_{\partial\Omega}\boldsymbol{\sigma}\cdot\mathbf{n}\,dA=0\\ \int_{\Omega}\left[\nabla\cdot\boldsymbol{\sigma}+\rho\mathbf{f}-\rho_s(1-\phi)\dot{\mathbf{v}}^s-\rho_f\phi\dot{\mathbf{v}}^f\right]\,d\Omega=0\\ \nabla\cdot\boldsymbol{\sigma}+\rho_s(1-\phi)(\mathbf{f}-\dot{\mathbf{v}}^s)+\rho_f\phi(\mathbf{f}-\dot{\mathbf{v}}^f)=0\end{aligned} \tag{2.9}$$

In the subsurface system, the body force $\mathbf{f}$ is gravity force $\mathbf{g}$. The quasi-static momentum balance for skeleton and fluid reads

$$\nabla\cdot\boldsymbol{\sigma}+\rho\,\mathbf{g}=0 \tag{2.10}$$

2.1.3. Constitutive Equations for Porous Material

In our study, isothermal conditions are assumed in the reservoir. In soil mechanics, the assumption of the incompressible matrix means that matrix (skeleton) undergoes negligible volume change. The latter assumption aids in deriving a constitutive equation that links the action of pore pressure exerted by pore fluid p and the stress tensor $\boldsymbol{\sigma}$ on the skeleton using Terzaghi's effective stress tensor $\boldsymbol{\sigma}'$, which can be written as:

$$\begin{aligned}\boldsymbol{\sigma}'&=\boldsymbol{\sigma}+\mathbf{1}p\\ \sigma'_{ij}&=\sigma_{ij}+\delta_{ij}\,p\end{aligned} \tag{2.11}$$

where $\mathbf{1}$ is the Kronecker delta function ($\delta_{ij}=1$ if $i=j$, otherwise $\delta_{ij}=0$). Note that the pore pressure acting on the skeleton through the internal walls of porous network results in the strain component.

The constitutive equation of linearised poroelasticity properties derived from state equations [25] can be written as

$$\begin{aligned}\delta\boldsymbol{\sigma}&=\mathbb{C}\,\delta\boldsymbol{\varepsilon}-b\;\mathbf{1}\;\delta p\\ \sigma_{ij}&=\mathbb{C}_{ijkl}\,\varepsilon_{ij}-b\;\delta_{ij}\;p\end{aligned} \tag{2.12}$$

where $\mathbb{C}$ is tensor of skeleton elastic stiffness moduli and b is Biot's coefficient.

For isotropic material, the Biot's coefficient b of linearised poroelasticity can be expressed in terms of Terzaghi's effective stress $\boldsymbol{\sigma}'$ in the case of compressible matrix using Biot's effective stress tensor $\boldsymbol{\sigma}''$. This constitutive relation can be written as

$$\begin{aligned}\boldsymbol{\sigma}''&=\boldsymbol{\sigma}+b\;\mathbf{1}\;p\\ \sigma_{ij}''&=\sigma_{ij}+b\;\delta_{ij}\;p\end{aligned} \tag{2.13}$$

Substituting eq.2.12 and eq.2.13 to eq. 2.11, the constitutive relation writes:

$$\boldsymbol{\sigma}=\boldsymbol{\sigma}'-\mathbf{1}p=\boldsymbol{\sigma}''-b\mathbf{1}p=\mathbb{C}\boldsymbol{\varepsilon}-b\mathbf{1}p. \tag{2.14}$$

This equation explains how Biot's effective stress be driving force of linearised elastic strain [25].

The symmetric strain tensor field $\boldsymbol{\varepsilon}$ can be derived from displacement field $\mathbf{u}$ and expressed as:

$$\begin{aligned}\boldsymbol{\varepsilon}&=\frac{1}{2}\left(\nabla\mathbf{u}+\nabla^{\mathrm{T}}\mathbf{u}\right)\\ \varepsilon_{ij}&=\frac{1}{2}\left(\frac{\partial u_i}{\partial x_j}+\frac{\partial u_j}{\partial x_i}\right)\end{aligned} \tag{2.15}$$

Since skeleton is the result of the matrix and porous media geometry, the constitutive relation between skeleton and matrix properties explains that the Biot's coefficient and the change of

volumetric strain ($\epsilon = \sum_i \epsilon_{ii}$) over skeleton are affected by porosity ϕ changes under isotropic linear poroelastic condition [25]:

$$\begin{aligned} d\phi &= b\ d\epsilon + \frac{dp}{N} \\ \frac{1}{N} &= \frac{b-\phi_0}{K_d};\ \ b = 1 - \frac{K_s}{K} \\ \phi &= \phi_0 + b(\epsilon - \epsilon_o) + \frac{(b-\phi_0)(1-b)}{K}(p - p_0) \end{aligned} \tag{2.16}$$

Here K denotes bulk modulus, K_s matrix bulk modulus and ϕ_0, p_o and ϵ_o are reference porosity, pressure and volumetric strain respectively.

The permeability field update in corresponding with porosity changes owing to deformation is written as[27] :

$$k = k_0 \left(\frac{\phi}{\phi_o} \right)^n \tag{2.17}$$

2.2. Fault Dynamics

In this section, it will be explained the governing equations controlling the dynamic of fault.

2.2.1. Poromechanics of Fault

In the continuum mechanics fault can be assumed as an embedded discontinuity of two planes that are in contact. Mechanical model of the fault can describe the stress (traction) and displacement along the fault. Figure 2.2 shows fault surface along with its mechanical parameters.

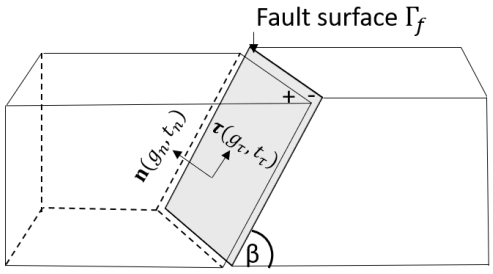

Figure 2.2: Illustration of fault surface in 3-D domain with fault dip angle β, reproduced after [2]

Each plane surface has its roughness (asperity) that would affect the behaviour of displaced planes (fig. 2.3a). The characteristic width of fracture contact is represented by g_o. Contact of surfaces without asperities is defined as ideal contact, where $g_o = 0$, see Fig. 2.3b for illustration. For modelling purpose, the roughness of the plane is being idealized in which zero thickness element will be used for finite element modelling. In mathematical modelling, the fault surface is considered as the boundary between two adjacent domains. The two opposing side of the fault surface is denoted as + and −. Note that normal vector of the fault $\mathbf{n}$ is pointing from the − to + side.

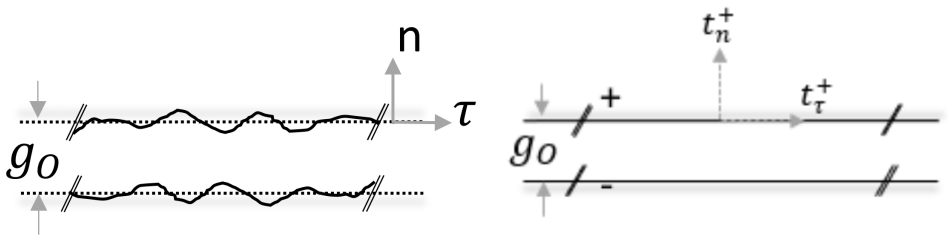

(a) Fault surface as contact with asperities (solid line) and idealised (dotted line)

(b) Traction forces acting on the fault surface with opening g_o

Figure 2.3: Representation of fault surface, reproduced after [3]

The motion of the contact boundary of fault surface is expressed by the relative displacements (positions) which is defined by gap function $g = (g_n, g_t)$ and can be mathematically written as:

$$\begin{aligned} d\mathbf{u} &= \mathbf{u}^+ - \mathbf{u}^- \\ g &= (d\mathbf{u})\begin{pmatrix}\mathbf{n}\\ \boldsymbol{\tau}\end{pmatrix} = (g_n, g_t) \end{aligned} \tag{2.18}$$

where + and − denote two sides of a fault surface, where u is a displacement vector.

In this relation, g_n is a normal displacement relative to the reference opening g_o, and g_t is the length of displacement vector parallel to fracture plane. Each contact constraint that is expressed regarding g_n has a characteristic solution as follows [28] :

- $g_n = 0$, contacts (fault surface) are not subjected from traction forces or stress;
- $g_n > 0$, contacts are under compression due to deformation (penetration);
- $g_n < 0$, no physical contact between the two side of fracture surface;
- $g_n = g_o$, is when fracture is completely sealed therefore in the normal gap, stress will be transmitted without alteration.

Traction forces or stress that act on the fault surface is related to full stress tensor, recalling Cauchy stress tensor (eq. 2.8) mathematically written as:

$$\mathbf{T} = \boldsymbol{\sigma} \cdot \boldsymbol{n} \tag{2.19}$$

In the fault coordinate system, traction is defined by projecting stress tensor $\boldsymbol{\sigma}$ on the normal vector $\mathbf{n}$ of the fault surface and can be expressed as:

$$\mathbf{t} = -\boldsymbol{\sigma}\ \mathbf{n} = t_n\ \mathbf{n} + t_t\ \boldsymbol{\tau} \tag{2.20}$$

where t_n is normal traction and t_t is shear traction. In this case, the traction forces on fault surface $\bar{\mathbf{t}}_f$ can also be expressed in terms of pore pressure and Terzaghi's effective stress $\boldsymbol{\sigma}'$ which is written as:

$$\bar{\mathbf{t}}_f = -\boldsymbol{\sigma}\ \boldsymbol{n} = -(\boldsymbol{\sigma}' - \mathbf{1}p)\ \boldsymbol{n} = t_n\ \boldsymbol{n} + t_t\ \boldsymbol{\tau} + p\ \boldsymbol{n}. \tag{2.21}$$

Similar to the displacement, for a designated fault opening, each surface side has its own traction force property written as (+,-). By using continuity condition, it can be assumed that the two opposite side of the fault surface shares the same traction magnitude, expressed following [3] as:

$$t_n^+ = t_n^- = t_n \tag{2.22}$$

$$t_t^+ = t_t^- = t_t. \tag{2.23}$$

The mechanical behaviour of fault is expressed by relationship between traction force and gap function, described in [28] as:

$$\begin{array}{lll} t_n = \mathcal{N}(g_n) & & \\ t_t = \mathcal{F}(t_n) & \text{if} \quad g_t \neq 0 & \text{for slip condition} \\ t_t < \mathcal{F}(t_n) & \text{if} \quad g_t = 0 & \text{for stick condition} \end{array} \tag{2.24}$$

Here $\mathcal{N}$ is a function that links normal traction t_n with normal gap g_n. The relationship between normal traction t_n and tangential traction t_t (shear) can be described using friction law $\mathcal{F}$ which also known as Mohr-Coulomb failure. The local displacement at the fault incorporated with frictional strength can be used to estimate the fault slip characteristic.

Note that the shear or tangential traction on the fault is limited by the fault friction (fault strength) under friction law $\mathcal{F}$, a criterion that can describe fault stick/slip conditions. Stick condition means the fault is stable, while slip means that the fault starts slipping or deformation starts to occur. Friction law is strongly related to fault failure criterion and will be explained next.

2.2.2. Fault Failure Criterion

In the earth subsurface, the three principal stresses consist of; vertical stress (σ_v), maximum horizontal stress (σ_H) and minimum horizontal stress (σ_h). These principal stresses govern the faulting regime of a region which are; normal, strike-slip and reverse faulting. The tectonic driving force and gravitational loading are contributing factors to the in-situ stress field. However, the magnitude of stress at depth cannot be exceeding the frictional strength of pre-existing faults.

The rock strength of pre-existing faults can be quantified with cohesion and frictional strength. At normal condition, the stress state is in equilibrium with rock frictional strength. A significant load of stress, either locally or globally, can cause fault to slip. In this study, pressure changes will result in stress change that further leads to fault reactivation.

In the equilibrium state, the principal stresses (σ_v, σ_H, σ_h) acting on porous media saturated by fluid, can be expressed in terms of Terzaghi's effective stress (σ_v', σ_H', σ_h') using equation2.11. The normal traction t_n and shear or tangential traction t_t that are acting on the fault surface can be expressed in terms of the effective principal stresses σ_1' and σ_3' applied on the rock [4] which can be written as:

$$t_t = 0.5(\sigma_1' - \sigma_3')\ sin2\beta, \tag{2.25}$$

$$t_n = 0.5(\sigma_1' + \sigma_3') + 0.5(\sigma_1' - \sigma_3')\ cos2\beta, \tag{2.26}$$

where β is the fault dip angle relative to horizontal plane. Note that for a normal faulting regime, σ_1' is the effective vertical stress (σ_v') and σ_3' is the effective minimum horizontal stress (σ_h'). Equations 2.25 and 2.26 indicate that increase in pore pressure may induce shear slip along the fault surface [10].

As rocks are being perturbed, the effective principal stresses would change leading to the deformation. Depletion perturbs the stress state since pressure decrease will increase stress. However, after depletion, the change in effective minimum horizontal stress ($\Delta\sigma_h'$) is a function of Poisson's ratio ν and the pore pressure change Δp. The change in effective vertical stress ($\Delta\sigma_V'$) remains proportional to pressure change. The relation between changes in the effective stress and the initial pore pressure Pp_0 after depletion writes:

$$\begin{aligned} \Delta Pp &= Pp_0 - Pp \\ \Delta\sigma_v' &= -\Delta Pp \\ \Delta\sigma_h' = \Delta\sigma_v' \frac{\nu}{(1-\nu)} &= -\Delta Pp \frac{\nu}{(1-\nu)} \end{aligned} \tag{2.27}$$

The equation 2.27 above describes that the slope of Mohr envelope increases as pore pressure decreases and the effective principal stress increases.

The Mohr-Coulomb failure criterion is developed by envelope curves from a series of deformation analysis (see Fig. 2.4a). The failure envelope can be linearized using the cohesive strength (cohesion) C_o and internal friction coefficient μ_i. The linearized Mohr failure intercepts at shear C_o at which normal stress is zero with the slope of the internal friction coefficient of intact rock μ_i. The internal friction coefficient of intact rock μ_i can also be expressed in terms of friction angle (ϕ), where $\mu_i = tan\phi$ (figure.2.4b).

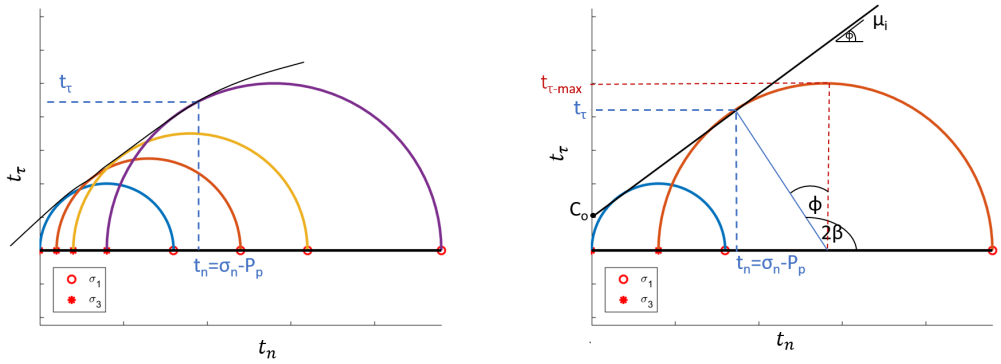

(a) Mohr failure envelop as a result of different stress

(b) Linearised Mohr-Coulomb failure

Figure 2.4: Mohr envelope to evaluate the fault failure processes for an intact rock or for critically stressed fault, reproduced after [4]

Figure 2.4b shows that shear stress is strictly limited to the fault frictional strength so it can never exceed the Mohr-circle [4] which is described as:

$$\mathcal{F} = t_{T_{max}} = C_o + t_n\mu_i = C_o + t_n tan\phi. \tag{2.28}$$

Here $t_{T_{max}}$ express maximum shear carrying capacity. For intact rock, fault starts to develop in the rock body as soon as failure criterion $\mathcal{F}$ is reached ($t_t \rightarrow t_{T_{max}}$) (see equation 2.24).

For rocks with pre-existing faults that is arbitrarily oriented, frictional sliding will be induced once the fault frictional strength exceeded its coefficient of static friction μ. According to Byerlee in 1978 based on a series of lab tests conducted, it stated that at elevated effective normal stress ($\sigma_v \geq \sim$10 MPa), fault friction is independent of its surface roughness, normal stress and rate of slip, such that the coefficient of friction is found to be within a relatively small range: $0.6 \leq \mu \leq 1$. This rule of thumb is then known as Byerlee's law [4, 10, 29].

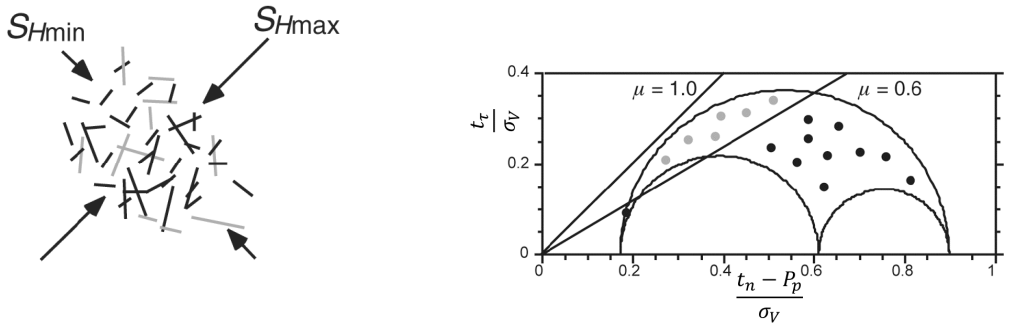

(a) Arbitrarily oriented fault as results of geologic processes and the current stress state

(b) Tractions that distinguish whether the fault is critically stressed (grey dots) or not

Figure 2.5: Arbitrarily oriented fault that is active and dead in the current stress field [4]

Figure 2.5a shows many faults with different orientations at depth. Each of these faults has its tractions acting on the fault surface whose magnitudes depend on the principal stresses, pore pressure and fault orientation. For a given value of minimum effective stress (σ_3), there is a maximum value that σ_1 cannot exceed. Again, this is governed by the frictional strength of the pre-existing faults ([29]). Figure 2.5b below shows the magnitude of shear and normal traction of the arbitrarily oriented fault plane. As the stress magnitude at depth varies, the Mohr diagram is normalised to the effective vertical stress σ_v. The grey dots correspond to tractions that lie on the coefficient of friction between 0.6 and 1.0, therefore, they are critically stressed and capable of sliding in the current stress field. The fault that is critically oriented

has an optimal angle for frictional sliding [4, 30] and can be written as:

$$\beta = \pi/2 - tan^{-1}\mu = 90 - \phi \tag{2.29}$$

The angle β is the angle between fault normal $\mathbf{n}$ and maximum effective stress σ_1. For normal faulting regime, angle β is equivalent to fault dip angle relative to the horizontal plane. The critically stressed fault tend to fail and is active in the current stress field.

Fault instability can be estimated by shear capacity utilisation (SCU), a ratio of shear stress t_t to failure criterion $\mathcal{F}$ of the fault surface which can be mathematically written as:

$$SCU = \frac{t_t}{\mathcal{F}} = \frac{t_t}{C_o + t_n tan\phi} \tag{2.30}$$

Equation 2.30 shows that decreasing pore pressure would de-stabilise fault and slip would occur by raising the ratio of shear to its maximum shear capacity on any pre-existing fault. Note that the role of pore pressure in frictional sliding is incorporated through the effective normal stress (normal traction), where $t_n + P_p$.

The fault slip condition can be established by the SCU number. The characteristics of SCU number are:

- SCU <1 : the fault is not slipping since shear stress lies below the friction envelope curve, therefore, fault behaves elastically;
- SCU = 1 : fault surface has reached its shear carrying capacity $t_{T_{max}}$ and starts to slip;
- SCU >1 : fault slipping due to $t_t > t_{T_{max}}$, local shear stress is redistributed to develop displacement along the fault (g_n, g_t) such that shear stress remains at the failure envelope curve. Fault behaves plastically under this condition.

To evaluate the mechanical behaviour of the fault, the characteristic of SCU number on the fault can be associated with equation 2.24.

2.2.3. Fault and Fluid Flow

The active fault acts as conduit for fluid flow. The capability of fault to allow fluid flow is depending on its conductivity C_f, a function of fault permeability k_f and fault aperture α_f. The permeability of can be quantified by [10]:

$$k_f \sim \frac{\alpha_f^2}{12} \tag{2.31}$$

Consequently, the volumetric flow rate through a fault can be written as:

$$Q = \frac{C_f}{\mu}\nabla P = \frac{\alpha_f^3}{12\mu}\nabla P \tag{2.32}$$

The fault conductivity C_f is quantified by *fault permeability* × *fault aperture*. As the fault aperture k_f is equivalent to gap normal g_n (see equation 2.18), thus, fault conductivity can be written as:

$$C_f = \frac{g_n^3}{12} \tag{2.33}$$

It is a function of effective normal stress or normal traction acting on the fault. The normal gap changes as a result of mechanical align, then the new fault conductivity can be evaluated according to [3, 10] as:

$$\Delta g_n = f \cdot \Delta u_N \tag{2.34}$$

$$C_f = \frac{g_n^3}{12} + C_{f,0} \tag{2.35}$$

where f is friction factor that represent asperity of fault surface, u_n is fault normal displacement and $C_{f,0}$ is the reference conductivity. Figure 2.6 shows the relationship of effective normal stress (normal traction) on the fault with normal gap and fault conductivity respectively.

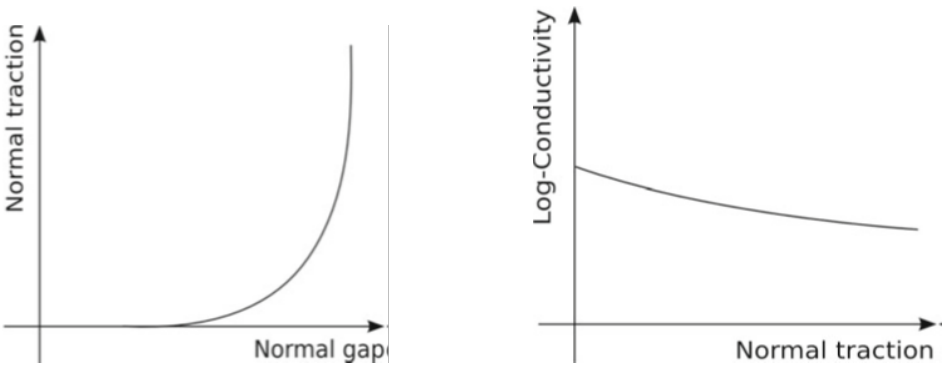

(a) Relationship between normal traction and gap normal

(b) Relationship between fault conductivity and normal traction

Figure 2.6: Relationship between normal traction with respect to gap normal and fault conductivity [3]

In the finite element method, Δu_N will determine the mechanics of the fault. Positive values of the normal gap and normal traction represent fault closure, where fault surface penetrates on to one another. For negative normal gap, the absolute g_n will be taken into account and associated with laminar flow through the fault surface. For zero normal gap, fault conductivity will only represent the surface contact with asperity[3].

3. Discretization and Numerical Solution

Description of how coupled of flow and mechanics being modeled in ADGPRS discussed in this chapter. The elaboration of the framework are adapted from [3, 5, 6].

The flow and and mechanics problem are coupled, however, the numerical methods that are used for numerical approximation are different. Flow equation is discretised using finite volume method and fault is incorporated using Discrete Fracture Model [5]. The mechanics problem is discretised using the finite element approach [3]. Nevertheless, both problems share the same unstructured grid so that the information exchange within the grid is easier. The coupled problem is solved fully implicitly using ADGPRS [6].

3.1. Grid Structure

The grid is created to capture physical entities of the rock system represented by geometrical structure. Figure 3.1 shows that the coupled problem are explicitly approximated using the same unstructured mesh. Although it represents physical domain in 2D, it is important to mention that for simulation in ADGPRS, the grid is constructed in 3D. In this work, the hexahedron mesh is used for matrix gridding and quadrangle mesh is used for gridding of fault surface.

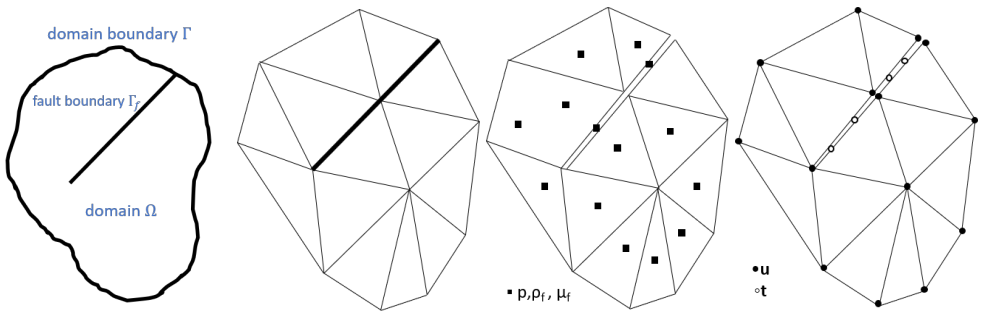

(a) Simplified physical domain of faulted rock (b) grid structure of the rock model (c) Grid structure for flow (d) Grid structure for mechanics

Figure 3.1: Flow and poroelasticity problem share the same grid structure. Fig 3.1c shows cell center properties for flow; p, ρ_f and μ_f. Fig 3.1d shows vertices carrying information of displacement vector **u** and Gauss points represent traction vector **t** on the fault surface. Figures are Re-illustrated after [3]

Figure 3.1a shows the idealised physical domain Ω whose represents matrix with the domain interface Γ and fault interface Γ_f. Figure 3.1b illustrates an example of gridding in physical domain by unstructured grid by having triangular mesh for matrix and bold line for fault. These mesh is used to approximate both flow and mechanics. Figure 3.1c depicts points where degrees of freedom are defined for flow problem using finite volume method with DFM. The nodes are positioned at the centroid of the control volumes. The properties associated

with cell center are pressure p, density ρ_f and viscosity μ_f. There is also property associated with cell interface such as velocity u. Figure 3.1d represents grid structure for mechanic problem where fault is defined as a contact between two surfaces of matrix elements. The displacement vector $\mathbf{u}$ is associated with grid vertices (black dots). Each nodes will keep track of displacement in each side of the fracture surfaces. Additionally, light dots are Gauss points correspond to traction vector $\mathbf{t}$ associated with fracture surface [3].

3.2. Discrete Fracture and Matrix Model

DFM model will be used to solve flow equation. It handles porous matrix and fracture as two different entities, hence, the treatment will differ for matrix-matrix, matrix-fracture and fracture-fracture connections. This includes discretisation of the matrix and fault separately and incorporating them to the flow equations. The flow solution is approximated in the unstructured grid using finite volume technique with two-point flux approximation.

The volumetric flow rate for two adjacent control volume (CV) writes

$$Q_{ij} = T_{ij}\lambda(P_i - P_j) \tag{3.1}$$

where Q_{ij} is flow rate between CV i and j, T_{ij} is the geometric transmissibility, $\lambda = \rho_f/\mu_f$ is fluid mobility, and $\Delta P = P_i - P_j$ is pressure gradient.

Geometric transmissibility is treated differently in matrix-matrix, matrix-fracture and fracture-fracture connections [5]. For matrix-matrix connection, geometric transmissibility can be written as:

$$\begin{aligned} T_{ij} &= \frac{\alpha_i \alpha_j}{\alpha_i + \alpha_j} \\ \alpha_i &= \frac{A_i k_i}{D_i} \mathbf{n}_i \cdot \mathbf{f}_i \end{aligned} \tag{3.2}$$

with A_i denotes the area of interface between two adjacent CV, k_i permeability of cell i, D_i distance between interface centroid and cell center, $\mathbf{n}_i$ vector normal of interface and $\mathbf{f}_i$ vector connecting centroid of interface and cell centre. Figure 3.2 below illustrates the components of geometric transmissibility between cell 1 and cell 2.

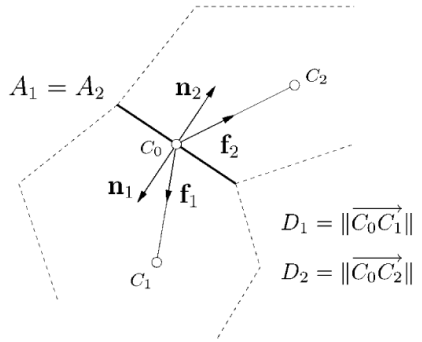

Figure 3.2: Geometric transmissibility representation between two adjacent cells [5]

The geometric transmissibility of fracture-matrix connection can also be computed with equation 3.2. However, the adjacent control volume (fracture-matrix) is distinct in terms of grid domain. The fracture thickness will be taken into account such that the fracture and matrix would have the same dimension and the connection would be easily established. Figure 3.3 shows the connection of fracture-matrix in grid domain and being transformed in computational domain to set up the geometric transmissibility in figure 3.2. Note that the fracture thickness is apparent and only defined in computational domain to simulate fluid flow. In the elasticity problem, the fault entity will be considered as zero thickness element.

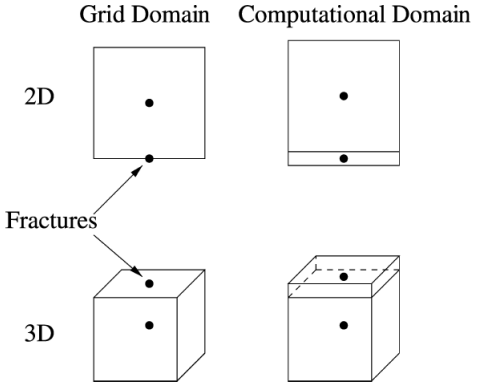

Figure 3.3: Illustration of fracture-matrix connectivity in grid and computational domain to set up the geometric transmissibility [5]

The connection between fracture-fracture CV is accomplished through an intermediate CV (CV_0). CV_0 is introduced for flow redirection and thickness adjustment. In general, flow can be considered as getting through three blocks in a series, that is: fracture CV_i to CV_0 and CV_0 to CV_j. To remove the intermediate CV_0, the transmissibility between fracture fracture CV (CV_i to CV_j) will then computed by taking the harmonic mean between each fracture CV and CV_0:

$$T_{ij} = \left(\frac{T_{i0}T_{0j}}{T_{i0} + T_{0j}}\right) \approx \left(\frac{\alpha_i \alpha_j}{\alpha_i + \alpha_j}\right) \tag{3.3}$$

assuming the size of intermediate CV is very small compared to adjacent CV. Then in CV_i, $D_0 \ll D_i$; $k_0 \simeq k_i$; thus $\alpha_0 \ll \alpha_i$ resulting in $T_{i0} \simeq \alpha_i$ and the same applies to CV_j. In this configuration, $\mathbf{n}_i \cdot \mathbf{f}_i = 1$. Figure 3.4 shows the fracture-fracture connectivity in 2D where 1 and 2 denote the fracture cells and 0 intermediate CV_0.

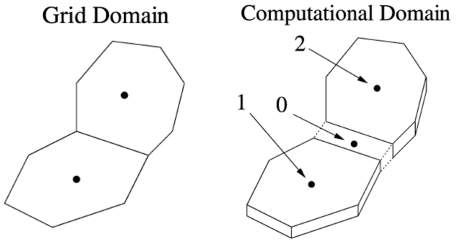

Figure 3.4: Illustration of 2D fracture-fracture connectivity in grid and computational domain through intermediate CV_0 to establish the geometric transmissibility [5]

As the flow problem will be solved implicitly, the backward Euler will be used for two points flux approximation in the time domain. Combining equation 3.1 and equation 2.4, the discretized flow equation can be expressed in residual form:

$$\frac{{\rho_f}_i^{n+1}\ \phi_i^{n+1} - {\rho_f}_i^{n}\ \phi_i^{n}}{\Delta\ t} V_i = \sum_j Q_{ij} + q_i V_i \tag{3.4}$$

where V_i is volume of i_{th} grid, j is summed over all neighboring CV, Δt is time step, superscript $n+1$ and n denote current and previous time step respectively. Using Euler Backward method, the right hand side of the equation is approximated at the current time step $n+1$. In addition, fault transmissibility and porosity are strongly dependent on the pressure and stress field (see eq. 2.32 and 2.16 respectively). They will be updated in fully implicit manner in accordance with pressure and stress field solutions. Note that the initial geometric transmissibility information is calculated at pre-processing stage and during the simulation is updated at every nonlinear iterations.

3.3. Fault Contact Constitutive Relations

Finite element approach is used for approximation of mechanics problem which includes an approximation of the contact problem on the fault.

In the finite element mesh, contact problem is treated as a simple two-node element on which one boundary node relative to the other boundary node is used to determine the displacement. The displacement vector in the finite-element is modelled based on the nodal analysis which model is approximated using shape function. Shape function is a function that interpolates the varying solutions between the mesh nodes. In the Galerkin's approach, shape functions use low order polynomial for interpolation which are defined at each node [31]. Finite element approximation of gap function in terms of displacement can be written as:

$$\mathbf{u}(\xi) \approx \sum_a N_a(\xi)\ \mathbf{u}_a \tag{3.5}$$

$$g(\xi) = \mathbf{u}^+(\xi) - \mathbf{u}^-(\xi) \approx \sum_a N_a(\xi)(\mathbf{u}_a^+ - \mathbf{u}_a^-) = \sum_a N_a g_a \tag{3.6}$$

where ξ is parametric coordinate, $\mathbf{u}$ is nodal coordinate displacement, N_a is shape functions of element, $\mathbf{u}^+$ and $\mathbf{u}^-$ are displacements of two side of fault surface.

Gap function and tractions acting on fault surface Γ_f can be associated and expressed in terms of computational nodes and elements with the given element of fault surface $\Gamma_{f,e}$ [3]:

$$\begin{aligned} &\int_{\Gamma_f} \delta g_n\ p\ d\Gamma - \int_{\Gamma_f} (\delta g_n t_n\ +\ \delta g_t t_t)\ d\Gamma \\ &\approx \sum_e \times \int_{\Gamma_{f,e}} \sum_a \delta(g_n)_a\ N_a\ p\ d\Gamma - \sum_e \times \int_{\Gamma_{f,e}} \left(\sum_a \delta(g_n)_a N_a t_n\ + \sum_a\ \delta(g_t)_a\ N_a t_t \right) d\Gamma. \end{aligned} \tag{3.7}$$

Here, gap and tractions are summed for every computational node a and element e. The traction vector $\mathbf{t} = (t_n, t_t)$ is computed for each Gauss Point on which fault element $\Gamma_{f,e}$ is associated with. Recall that pore pressure P_p effect can be included in the normal direction of the fault approximated by adding extra term to normal traction $t_n - P_p$. Pore pressure will be a piece-wise constant on fault element $\Gamma_{f,e}$. In the case of the fault opening, the two side of the fault surface will loose physical contact, consequently the traction term will be diminished, therefore, only pore pressure term will act on fault surface.

In numerical approximation, the fault traction is treated as an ideal contact condition on fault surface Γ_f using Kuhn-Tucker relations for Mohr-Coulomb friction law:

$$\begin{aligned} t_n \geq 0,\ \ g_n \geq 0,\ \ t_n \cdot g_n = 0, \\ \Phi \leq 0, \\ \dot{g}_T(\xi) - \eta \frac{\partial}{\partial t_t}\Phi = 0, \\ \eta \geq 0,\ \ \eta\Phi = 0. \end{aligned} \tag{3.8}$$

with $\Phi = |t_t| - \mathcal{F}(t_n)$ is a yield function that can only be zero or negative, as stated in the second line of equation 3.8. The first line describes that normal opening (gap) would occur if normal traction t_n is zero. The third and fourth line express that slip will take place when $\Phi = 0$ andshear slip g_t directed opposite to t_t. It can also be inferred that stick condition applies once $\Phi < 0$ (consequently, $|t_t| < \mathcal{F}(t_n)$) and $\dot{g}_T = 0$.

Tractions on the fault surface govern contact slip/stick conditions. Imposing such constrain conditions to nodal pair (element), in which the gap g is evaluated, can be approached with three methods: Lagrange multipliers, penalty method, and augmented Lagrangian method. The Kuhn-Tucker constrains and stick-slip condition can be rewritten by means of penalty

method:

$$\begin{aligned} t_n &= \varepsilon_N g_n, \\ \dot{g}_T - \eta \frac{\partial}{\partial t_t}\Phi &= \frac{\dot{t}_T}{\varepsilon_T}, \\ \eta \geq 0, \quad \Phi \leq 0, \quad \eta\Phi &= 0, \end{aligned} \tag{3.9}$$

with penalty parameters of $\varepsilon >> 1$ and $\varepsilon_T >> 1$. The first line of the equation state that under compression, $t_n > 0$, penetration takes place, $g_n > 0$. Fault starts to be stress-free contact when $\varepsilon_N >>$ such that normal gap is slightly opened $g_n \approx 0$.

For the fault surface with asperities, contact area is proportional to forces acting on the fault surface during deformation. Barton [32] proposed a relationship for normal contact forces that incorporating asperities in terms of initial normal stiffness k_n:

$$\mathcal{N}(g_n) = \frac{k_n g_0}{g_0 - g_n} g_n. \tag{3.10}$$

Therefore, relationship of normal traction and gap normal can be rewritten as:

$$t_n = \mathcal{N}(g_n), \quad g_n \leq g_0 \tag{3.11}$$

The traction vector is then computed using return mapping algorithm [3, 33]:

$$t_n^{n+1} = \mathcal{N}\left(g_n^{n+1}\right) \tag{3.12}$$

$$t_t^{trial} = t_t^n + \varepsilon_T \left(g_t^{n+1} - g_t^n\right) \tag{3.13}$$

$$\Phi^{trial} = \left|t_t^{trial}\right| - \mathcal{F}\left(t_n^{n+1}\right) \tag{3.14}$$

$$if\ \Phi^{trial} \leq 0;\ t_t^{n+1} = t_t^{trial} \tag{3.15}$$

$$if\ \Phi^{trial} \geq 0;\ \left|t_t^{n+1}\right| = \mathcal{F}\left(t_n^{n+1}\right) \tag{3.16}$$

where $\mathcal{N}$ is normal contact forces, $\varepsilon_N; \varepsilon_T$ are penalty parameters, superscript n and $n+1$ are previous and current time step respectively.

3.4. Coupling Strategies

The fully implicit coupling of flow and mechanics is performed in our study. It means that the physics of flow and mechanics are solved simultaneously. The solution of each module is expressed in residual form, where the unknown vector x and its corresponding residual R are introduced:

$$\begin{aligned} x &= (x_F, x_M) \\ R_F(x_F, x_M); R_M(x_F, x_M) \end{aligned} \tag{3.17}$$

Here x_F and x_M denote flow and mechanical unknowns respectively while R_F and R_M are the corresponding residuals.

The residual of single phase flow equation are derived from mass balance equation 2.4 as:

$$R_F \equiv \frac{\partial}{\partial t}\left(\phi \rho_f S_f\right) + \nabla \cdot \left(\rho_f \left(-\frac{\mathbf{k}}{\mu_f}\right)\right) + \rho_f q = 0 \tag{3.18}$$

The unknowns in flow problem are fluid pressure p_f and saturation S_f. The residual of mechanics are derived from momentum balance (eq: 2.10):

$$R_M \equiv \nabla \cdot \sigma + \rho g = 0, \tag{3.19}$$

with primary unknown is displacement u.

The fully implicit coupling will solve all the residual equations simultaneously, expressed as[6]:

$$\begin{cases} R_F^{n+1}(x_F^{n+1}, x_M^{n+1}, x^n) & = 0 \\ R_M^{n+1}(x_F^{n+1}, x_M^{n+1}, x^n) & = 0 \end{cases}$$

The residuals are then linearized using Newton's method that can be written in matrix form:

$$\begin{bmatrix} \partial R_F/\partial x_F & \partial R_F/\partial x_M \\ \partial R_F/\partial x_M & \partial R_M/\partial x_M \end{bmatrix} \begin{bmatrix} \delta x_F \\ \delta x_M \end{bmatrix} = - \begin{bmatrix} R_F \\ R_M \end{bmatrix}$$

Some of the physical properties are governed by more than one physical module. In this case, porosity ϕ is a function of pressure p in flow subset and volumetric strain ε_v as well as mean stress σ in mechanics subset. This coupled property will be calculated first for every iteration and later followed by other physical properties of each subset. Once the corresponding subset is updated, the coupled property will be re-updated.

Figure 3.5 is showing the general framework of current ADGPRS version.

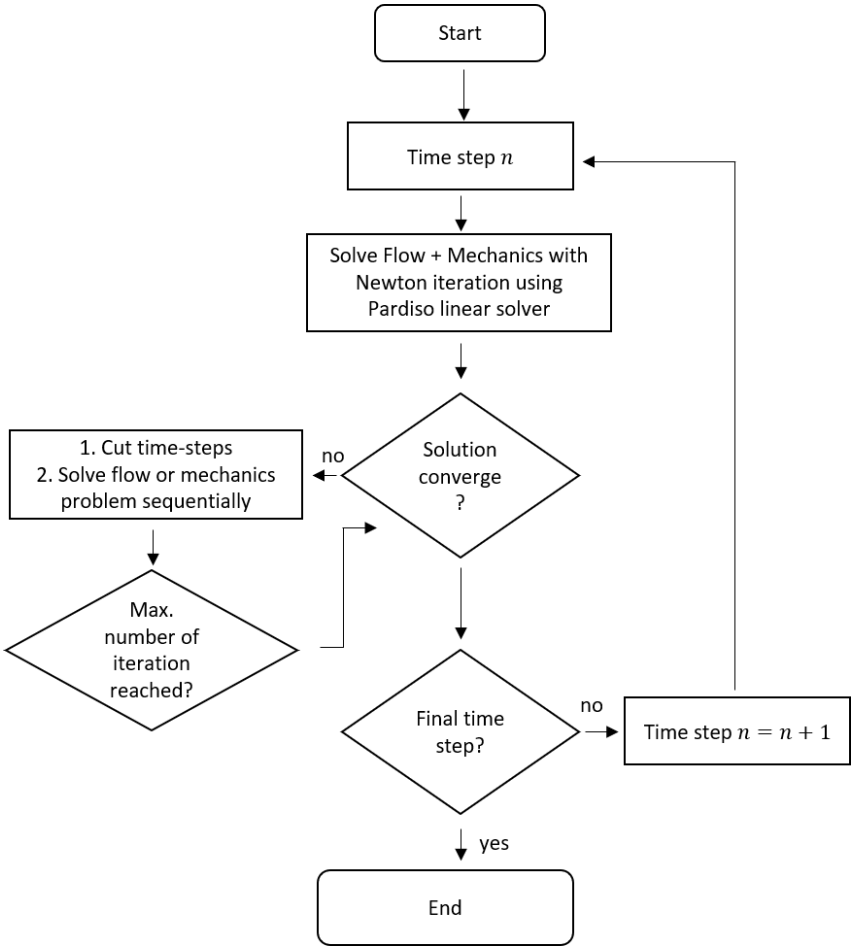

Figure 3.5: General framework of ADGPRS [6]

During the simulation, the mechanics status of slip/stick condition of the discretised element will be reported by ADGPRS using two numbers; 0 if the element is at stick condition and one is at slip condition.

4. Model validation

The model was constructed to reproduce the results from the NAM report about various modelling options on the fault slip response written by P.A.J. Bogert [7]. In their work, authors used a very accurate mechanical model which can capture the mechanical dynamic of fault reactivation quite precisely with modeling using 2-D Diana FEA (Finite Element Analysis). Recently, publication discuss the model was extended extended to rupture dynamics[8]). However, the production dynamics was not fully covered in their work and was incorporated as a step-wise pressure drop discrete in time. For this reason, their model used in [7] has limitation in estimating of production impact on fault reactivation.

In our work following the model used in [7], the simulation is performed by full coupling of flow and geomechanics using ADGPRS simulator. The fault behaviour due to depletion with different fault offset (fault throw) will be compared to [7]. The offset variability that will be simulated are; no offset (0 m fault throw); 80 m offset; 215 m offset; and 440 m offset.

The fault presence is dividing the block model into two parts, hanging wall and footwall. The major assumption in this model is that the fault is sealed. Both hanging wall and footwall block are depleted at the same rate.

4.1. Model Setup

In this section, a brief description of the model geometry and parameters that is used in NAM report [7].

4.1.1. Model Geometry

The setup is adopted from [7] that is a simplified geometry of Groningen subsurface as explained in chapter 1. The model is extended 2000 m wide and 1000 m broad. The model geometry is specified in table 4.1.

Table 4.1: Model Geometry

	Top [m]	Bottom [m]	Thickness [m]
Over-burden layer	-2500	-2780	2780
Cap rock (ZEZ 1)	-2780	-2830	50
Reservoir layer (ROSL)	-2830	-3045	215
Under-burden Layer (Limburg)	-3045	-3500	2955
Width x [m]	2000		
Breadth y [m]	1000		
formation offset /throw [m]	0; 80; 215; 40		
fault dip with respect to horizontal [deg]	65		

The model geometry along with its mesh was created using gmsh program [22]. The grid shapes are irregular quadrangles for the faces and hexahedron for the control volume. The mesh refinement is created towards the reservoir layer and fault surface in order to resolve the

properties and simulation result better. The figure below shows the model for different layer created with gmsh.

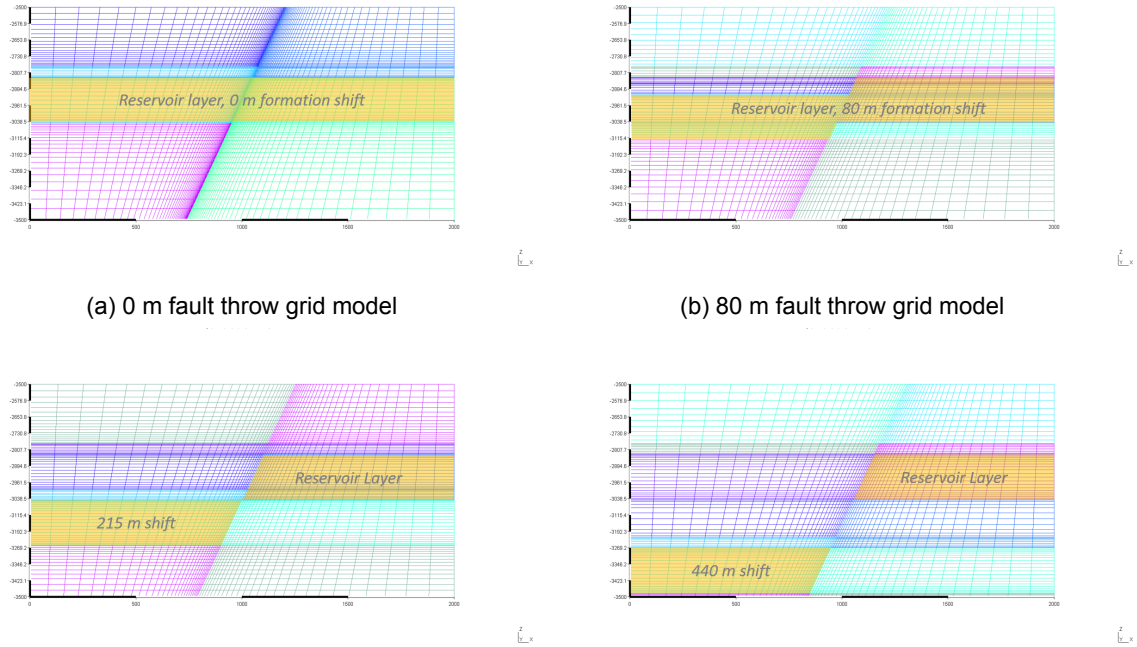

(a) 0 m fault throw grid model

(b) 80 m fault throw grid model

(c) 215 m fault throw grid model

(d) 440 m fault throw grid model

Figure 4.1: Grids of model geometry for various fault throw, generated by gmsh

4.1.2. Formation Properties

The rock properties defined in [7] and adopted in our work are present in table .

Table 4.2: Rock properties

	Underburden (Limburg)	Reservoir (ROSL)	Cap rock (ZEZ1)	Overburden Layer
ϕ	0.05	0.2	0.0001	0.05
Kv [mD]	1.00E-10	150	1.00E-12	1.00E-10
Kh [mD]	1.00E-11	15	1.00E-13	1.00E-11
ρ [kg/m^3]	2700	2450	2450	2172
b	1			
E [Pa]	1.00E+10			
ν	0.25			
Cr [bar^{-1}]*	1.50E-05			
SV Gradient [Bar/m]	0.214			
SHmax Gradient [Bar/m]	0.171			
Shmin Gradient [Bar/m]	0.16			
Sh_{min}/S_v	0.748			
Sh_{max}/S_v	0.795			

Here E is Young Modulus, ν Poisson's ration, b Biot's constant, C_r rock compressibility. The overburden stress S_v is cumulative of the formation weight from surface to depth z, mathematically written as:

$$S_v = \sum_{i=1}^{n_r} \rho_i g z \tag{4.1}$$

The parameter marked with asterisk in the table above, in this case is rock compressibility, was manually computed using the given Poisson's ratio ν and young modulus E. Rock compressibility C_r can be calculated by:

$$C_r = \frac{3(1-2*\nu)}{E} = \frac{3(1-2*0.25)}{1e10}\ Pa^{-1} = 1.5e-10\ Pa^{-1} = 1.5e-5\ Bar^{-1} \tag{4.2}$$

4.1.3. Fluid Properties

The fluid properties defined for simulation are shown in table 4.3.

Table 4.3: Fluid properties

Overburden	Pressure Gradient [bar/m]	0.1
	Pore Pressure [bar]	1.01+0.1D
Cap rock (ZEZ 1)	Pressure Gradient [bar/m]	0.1
	Pore Pressure [bar]	1.01+0.1D
Reservoir (ROSL)	in situ gas gradient [bar/m]	0.018
	Gas-bearing zone Pressure[Bar]*	298.09 + 0.018 D
	GWC - TVD [m]	2995
	GWC - P [bar]	352
	Water-bearing zone Pressure[Bar]*	0.117 D + 1.01
Underburden (Limburg)	Pressure Gradient [bar/m]	0.1166
	Pore Pressure [bar]	1.01+0.1166D
Water Properties	Density at Surface[kg/m^3]	1225
	Viscosity [cP]	0.511
	Bw at P = 1 Bar	1
	Cm [bar-1]	1.00E-06
Gas Properties	ρ at Surface	0.835
	Viscosity [cP]	0.061
	Bg at P = 1bar	1.0
	Bg at P = 1000bar	0.09

The pore pressure in the reservoir layer was not explicitly specified. Instead, pressure and depth at gas water contact (GWC) are defined. Above the GWC, the pore fluid is filled with gas whereas water is below GWC water. As GWC pressure and depth is known, pressure gradient below and above gas water contact in the reservoir layer can be estimated by using pressure-depth relationship. The gas pressure and water pressure are equal at the GWC depth, that is GWC pressure [26]. Therefore, at gas-water contact:

$$P_g = P_w = P_{GWC} \tag{4.3}$$

The linear equation for gas pressure above the gas water contact can be written as:

$$P_{gas} = \text{gas}\ \ \text{gradient}\ \times \text{depth} + \text{constant} \tag{4.4}$$

At GWC, 2995 mTVD and P_{gas} = 352 Bar, using hydrostatic pressure assumption, therefore the pore pressure gradient of gas bearing zone is defined as:

$$\begin{aligned} P_{gas} &= \frac{dP}{dD}_{gas} \times D_{GWC} + C = P_{GWC} \\ P_g &= 0.018\left[\frac{Bar}{m}\right] \times 2995[m] + C = 352Bar; \\ C &= 298.09\ Bar; \\ P_g &= 0.018\left[\frac{Bar}{m}\right] \times 2995[m] + 298.09 = 352Bar \end{aligned} \tag{4.5}$$

At initial conditions when the reservoir is neither over- nor under-pressured, water pressure

at any depth can be estimated as:

$$P_{water} = \text{water gradient } \times depth + P_{atm} = \frac{dP}{dD}_{water} \times D + 1.01325\ bar \tag{4.6}$$

Below the gas water contact, the water gradient is estimated as:

$$\begin{aligned} P_{water} &= \frac{dP}{dD}_{water} \times D_{GWC} + 1.01Bar = P_{GWC} \\ P_w &= 2995[m] + 1.01Bar = 352Bar; \\ \frac{dP}{dD}_w &= 0.117\left[\frac{Bar}{m}\right]; \\ P_w &= 0.117\left[\frac{Bar}{m}\right] \times D_{GWC} + 1.01Bar \end{aligned} \tag{4.7}$$

4.1.4. Fault Properties

The fault behaviour after failure is ideal plasticity. The fault failure criterion is depending on the cohesion and friction angle. Greater value of cohesion and friction angle will fail with larger pressure perturbation. The fault is set to be sealing and defined with zero conductivity. The fault properties used for simulation are described in table 4.4.

Table 4.4: Fault properties

Cohesion [Bar]	70
Friction Angle [Deg]	10
Conductivity [m.mD]	1E-12

4.1.5. Well Parameter

The sealing fault is dividing the block model into two parts: hanging wall block and footwall block. Both blocks are depleted with the same production rate as designed in [7]. Well index is incorporated into the connection of control volume through transmissibility. The simulation was restricted to production rate control of 10,000 m^3/d, with reservoir pore volume of 8.6E7 m^3. Once BHP limit of 50 bar is reached, then the simulation is switched to BHP control. The well locations and parameters are defined in table 4.5.

Table 4.5: Well Parameter

Well 1 Coordinate	(± 500, 500, 2950-2850)
Well 2 Coordinate	(± 1500, 500, 2950-2850)
Well Index [cP-rm^3 /day-bar]	5
Rate [sm^3/day]	1.00E+04
BHP control [Bar]	50

4.2. Initial Condition

The gridded model has control volumes in which physical properties are stored. The initial conditions that vary with respect to depth defined for each control volume are:

1. Pore pressure. Pore pressure varies with respect to depth. The initial pore pressure is hydrostatic with the given gradient and intercepts at atmospheric pressure at the ground surface. The reservoir layer is over-pressured and the pressure of gas bearing zone was computed in equation 4.5 resulting in an approximation of initial reservoir pressure about 350 bar.
2. Initial Stress. As the model geometry is defined from depth 2500m TVD, overburden stress is defined on the top boundary using the vertical stress gradient. The minimum and maximum horizontal stress are computed by their ratio to vertical stress.

Since the block model is subjected to the principal stresses, traction forces acting on the fault surface are defined as a boundary condition. Other static properties are defined in tables 4.2-4.4 and will be taken into account for initialization in ADGPRS simulation.

The initial conditions of pressure and stress are plotted in figure 4.2. The dotted-lines are the numerical approximations and overlain on the analytical estimation. For the initial vertical stress (bottom of fig.4.2), the analytical data are estimated from two given information; in-situ stress gradient (dashed-line) and formation weight (solid-line), both of which are defined in table 4.2. Similarly, the horizontal stresses are analytically computed by the in-situ stress gradients (dashed-line) as well as ratio Sh_{max}/S_v and Sh_{min}/S_v (solid-lines). The numerical results fall in between the two analytical estimations.

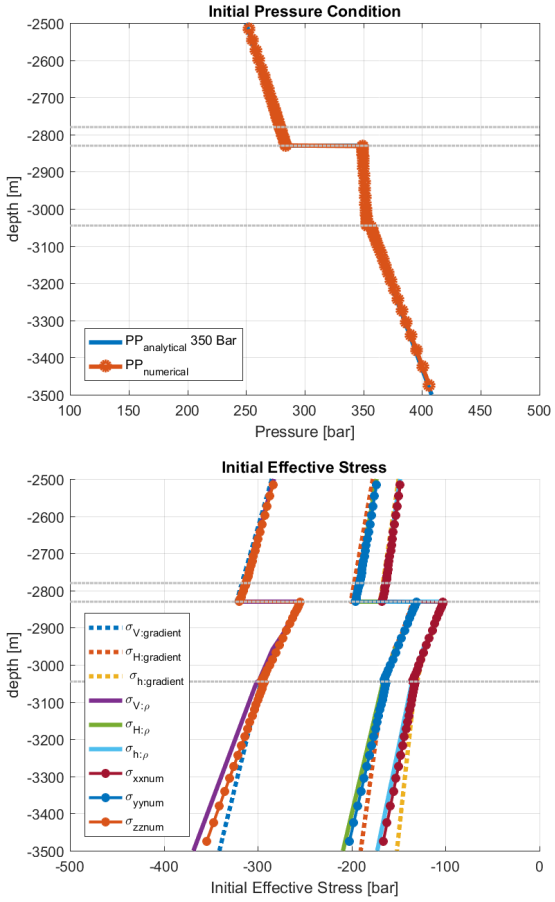

Figure 4.2: Initial condition of pressure and effective stress field

4.3. Modeling Result

The modelling results will be grouped into four different cases depending on the fault offset: 0 m, 80 m, 215 m and 440 m, and each of the cases will be compared to the results from the NAM report [7]. While the report discusses pore pressure depletion from initial reservoir pressure 350 bar down to 50 bar with a decrement of 50 bar, ADGPRS simulates the depletion process based on the fixed rate control with simulation period of 5000 days. Eventually, the simulated time can be associated with reservoir pressure after depletion. It is important to note that simulations in [7] are performed in 2D and only consider the geomechanical behaviour, while ADGPRS simulates the model in 3D and full coupling of flow and geomechanics is considered.

The figure 4.3 shows ADGPRS simulation pressure profile in flow and mechanical problem at different timesteps compared with the analytical solution. Based on this figure, the pore pressure output from coupled simulation of flow and geomechanics have the same values which proves that coupling is resolved in the model.

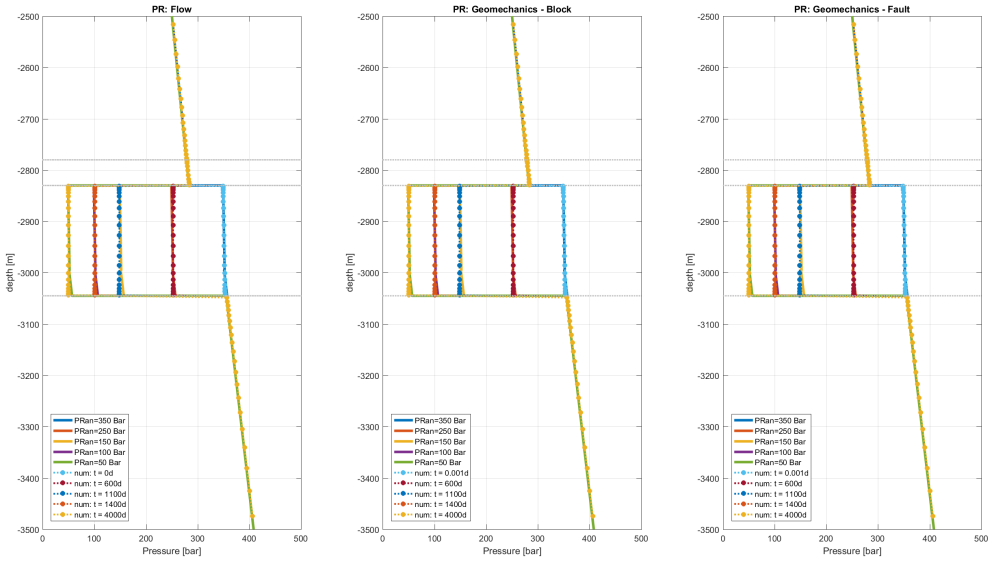

Figure 4.3: Comparison of reservoir pressure computed analytically (solid line) and numerically by ADGPRS (dotted line) for coupled flow and geomechanics for 0 m fault shift

As the reservoir is depleted, the effective stress state is also changing as a function of pressure. Figure 4.4 is the illustration of initial effective stress with pore pressure around 350 bar and final effective stress at which the final pore pressure is 50 bar.

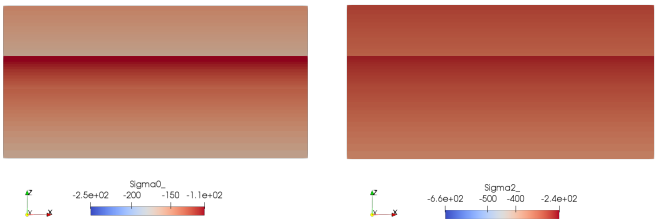

(a) Initial effective stress

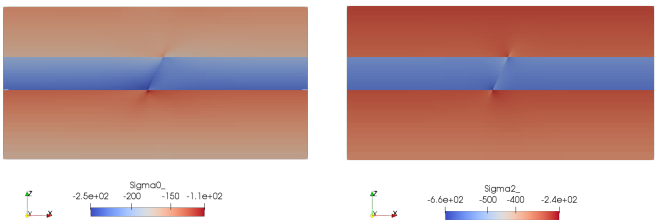

(b) Final effective stress

Figure 4.4: Distribution of the effective stress ($\sigma\prime$) on the block model at initial (top) and final time step (bottom) as results of pressure depletion. Sigma0 denotes effective stress in x-direction ($\sigma_{h_{min}}\prime$) and Sigma2 in z-direction ($\sigma_V\prime$).

Figure 4.4 shows the stress concentration along the fault in the reservoir layer. When pressure drops the lateral stress become redistributed above and below the reservoir, and this redistri-

bution is more pronounced due to fault presence. Stress subjected to the model subsequently lead to a change of tractions acting on the fault surface, in both normal and tangential direction. Once the shear stress acting along the fault exceeds its maximum shear capacity, the fault starts to deform and slip takes place. The deformation can be quantified by the displacement. Figure 4.5 shows a 2D displacement in the simulation model during the depletion.

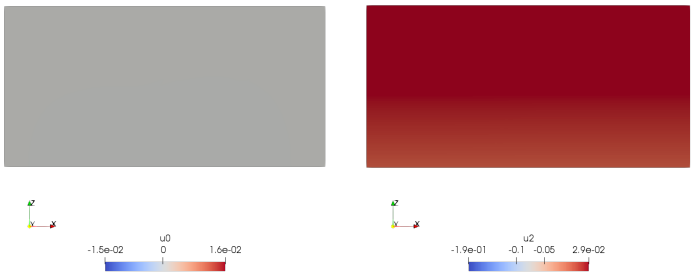

(a) Initial displacement

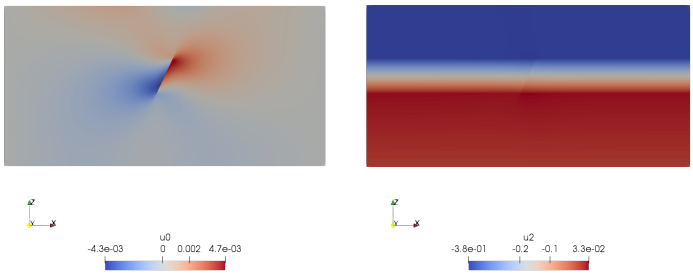

(b) Displacement at 2200 days

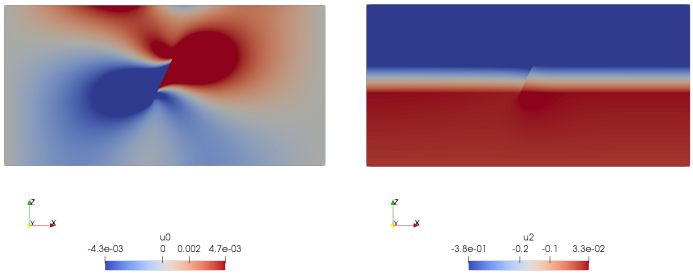

(c) Final displacement (4000 days)

Figure 4.5: 2D illustration of displacement during pressure depletion. U0 denotes displacement in x-direction and U2 displacement in z-direction.

According to figure 4.5, displacement evolution occurs once the stress and pressure are perturbed. In general, as the reservoir is being depleted, it can be interpreted that the formations above the reservoir are displaced downwards, whereas, the formations below the reservoir layer are displaced upwards. In addition to vertical displacement along the fault, the top of reservoir layer in the foot-wall block moves upward while the bottom of the reservoir in the hanging-wall block moves downwards. This behaviour proves that the stress state is under the normal faulting regime system where the down-thrown block goes down, and the up-thrown block goes up. The trend of lateral displacement along the fault is showing that foot-wall block and hanging wall block are moving away and fault opening would occur.

4.3.1. 0 m fault shift

The fault behaviours during depletion can be quantified by pressure, tractions (effective normal and shear stress), shear capacity utilisation (SCU) and relative shear displacement (RSD).

The comparison of pressure along the fault predicted in our study to the reference results [7] is depicted in figure 4.6. The grey dashed line marks the formation layering.

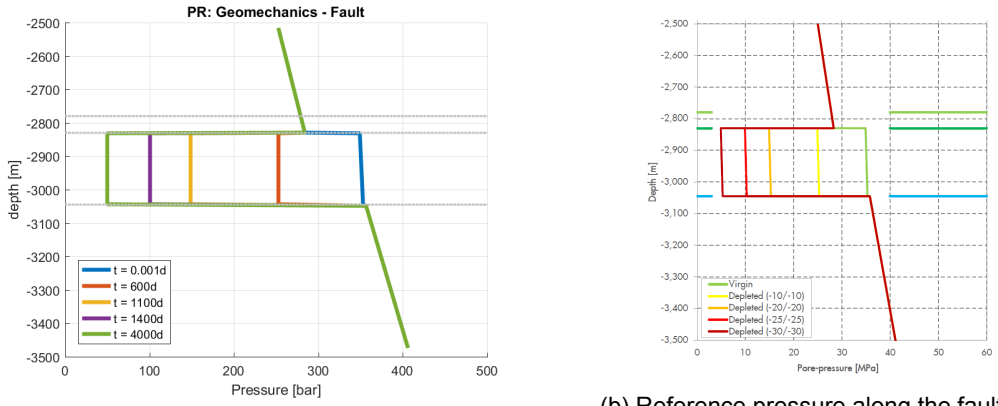

(a) Pressure along the fault simulated by ADGPRS

(b) Reference pressure along the fault [7]

Figure 4.6: Comparison of formation pressure during depletion between ADGPRS simulation and reference solution [7]

Tractions acting on the faults is a function of stress, which is dependent on pressure. The plot of tractions response normal and tangential to the fault surface is in figure below and the ADGPRS simulation result is being compared side-by-side with reference results [7]. It is clear that both results are in good agreement.

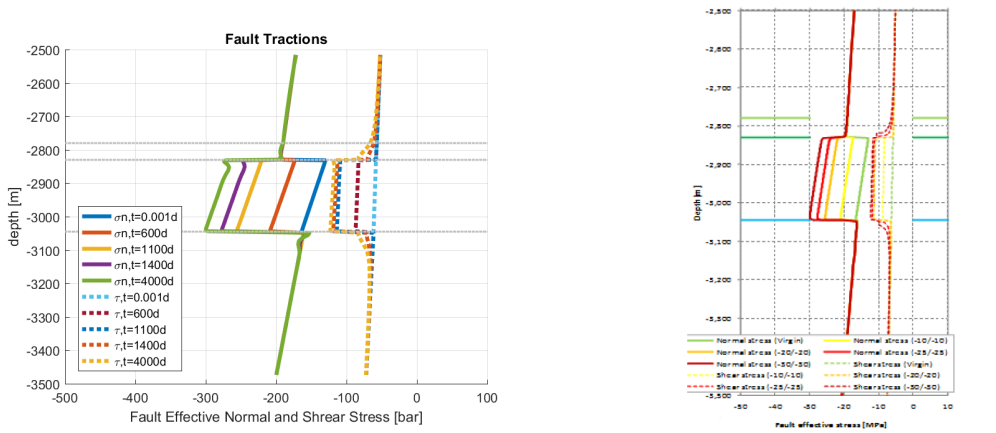

(a) Tractions simulated by ADGPRS

(b) Reference tractions [7]

Figure 4.7: Tractions acting on the fault. Simulated tractions is compared with reference results [7]. The solid line is the normal traction and dashed line is tangential.

The value of tractions determines whether a fault reaches failure with the given cohesion and frictions. Once shear acting on the fault reaches its maximum shear capacity, the fault will fail and slip along the fault is developed. The maximum shear capacity is quantified by shear capacity utilisation (SCU) which values cannot be greater than one (see eq. 2.30). Figure 4.8 shows comparison between our simulation result and reference solution [7].

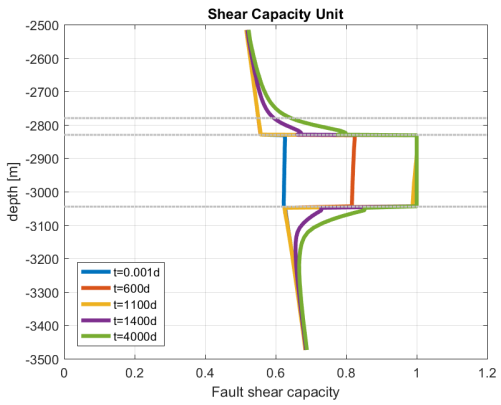

(a) SCU from ADGPRS result

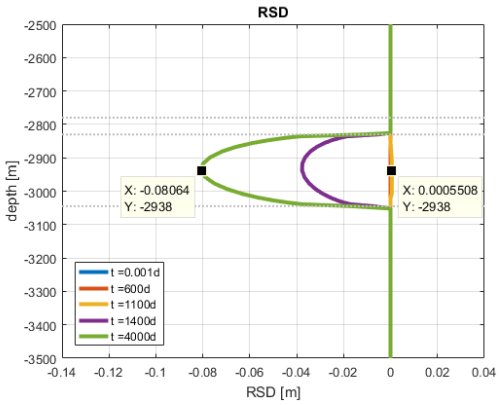

(b) RSD from ADGPRS result

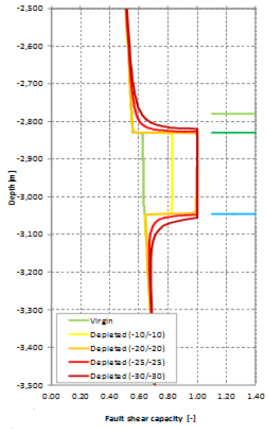

(c) Reference SCU [7]

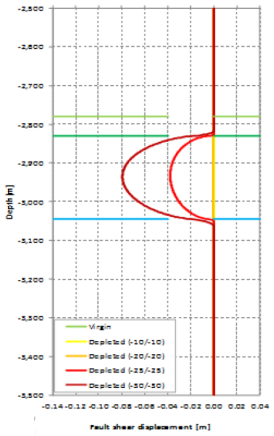

(d) Reference RSD [7]

Figure 4.8: ADGPRS simulation results of SCU and RSD in comparison with the reference [7]

From the figure. 4.8a it is clear that the SCU changes from non-permeable formations to reservoir is gradual.This occurs due to stress concentration effect that subsequently induced tractions and makes SCU at the top and bottom of reservoir boundary noticeable. RSD is already developed at 1400 (pressure 100 bar) with a maximum magnitude of 0.5 mm in the centre of the reservoir layer. Moreover, the maximum RSD is 0.08 m, and it is reached at reservoir pressure 50 bar.

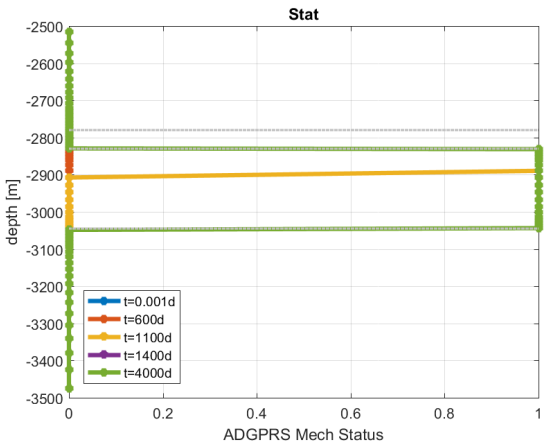

Figure 4.9: The mechanics status reported by ADGPRS during simulation

Figure 4.9 illustrates the mechanics status that is reported during ADGPRS simulation, where one means that fault failure criterion is reached and the displacement has started. Based on the reported status, fault slip takes place at 1100 day of simulation. Additionally, the reported mechanic status shows that fault fails from the top of the reservoir and propagates downwards. Figure 4.8a also shows that SCU value reaches one at 1100 days that corresponds to pore pressure 150 bar. However, the magnitude is very low and cannot be seen in comparison to RSD developed at the later time. The reservoir pressure at which fault fails is in accordance with the reference report ($\approx$ 19.9 MPa) which is equivalent to the pore pressure 15.1 MPa ($= 35 - 19.9$ MPa).

4.3.2. 80 m fault shift

Next, we compare our simulation results for the reservoir with an offset along the fault to the reference result [7]. The reservoir offset in this example is 80 m, that is less than half of the reservoir thickness 215 m. The reservoir is still juxtaposed to reservoir layer, as seen in figure 4.1b. The upper reservoir in the foot-wall block is juxtaposed to cap rock and over-burden, meanwhile, the lower part of the reservoir in the hanging-wall block is juxtaposed to under-burden formation.

The pressure response, tractions, SCU and RSD results along the fault simulated by ADGPRS are illustrated in figure 4.10 below, meanwhile the reference results [7] as are shown in the appendix A, figure A.1.

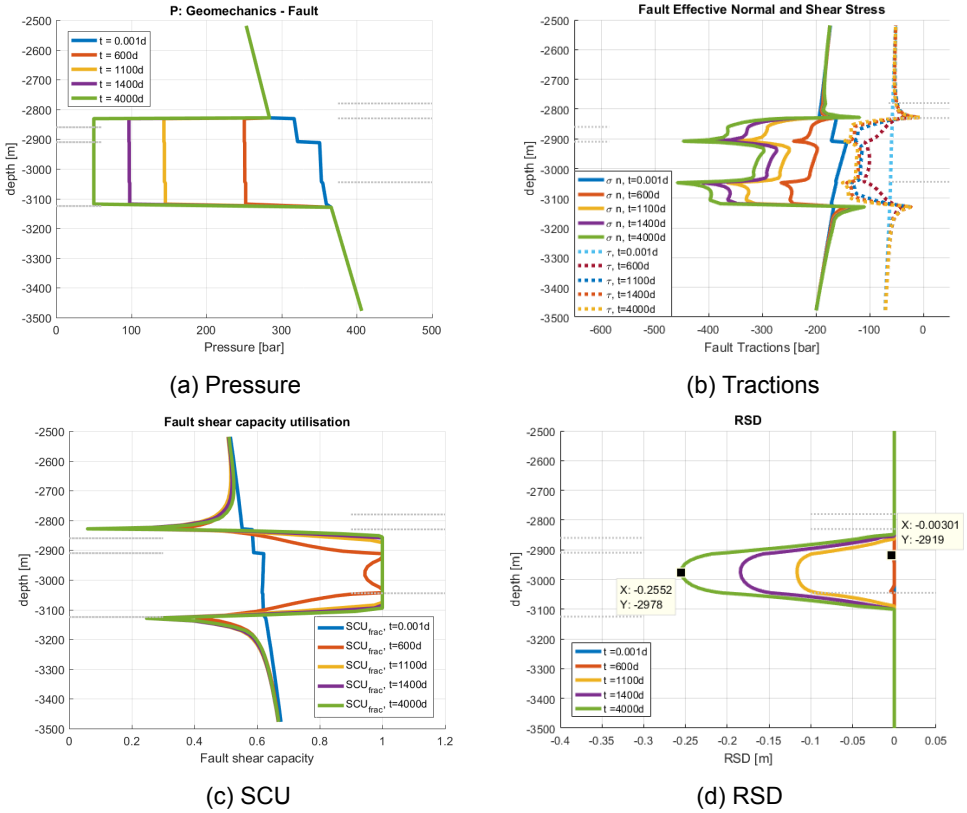

(a) Pressure (b) Tractions

(c) SCU (d) RSD

Figure 4.10: ADGPRS simulation results for 80 m fault offset

In the case when the offset is 80 m, the fault failure begins to develop at 600 simulation days that corresponds to pore pressure 250 bar. This is marked by a tangential gap (RSD) less than 0.01 m. However, in the early failure the fault only fails at the top hanging wall and base of footwall. This is because effective stresses are concentrated on the fault when the reservoir is not juxtaposed to reservoir layer. As seen in figure 4.11, the stress concentration can be seen on upper and lower fault of the reservoir layer. This phenomena induces greater tractions acting on the top of hanging wall and base of footwall of fault surface which can be seen in Fig. 4.10b.

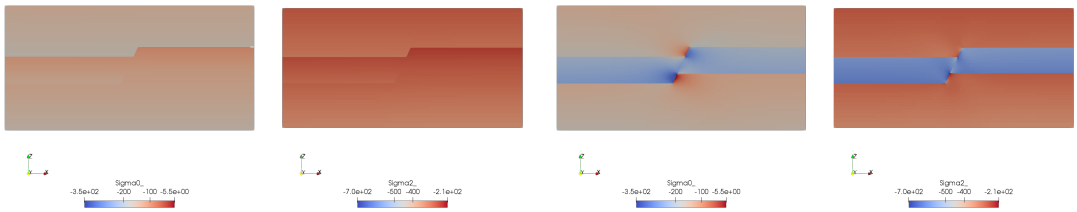

(a) $\sigma_{h_{min}}'$ (left) and σ_v' (right) at initial time step (b) $\sigma_{h_{min}}'$ (left) and σ_v' (right) at final time step

Figure 4.11: 2D effective stress σ_1' and σ_3' distribution over the block model at initial and final time

.

The fault starts failing at earlier depletion compared to the case with no offset fault. This is because a larger area of fault is exposed to depletion and even small pressure perturbation can trigger fault slip. In general, the displacement magnitude is greater with non-zero offset fault. At the later stage of failure, maximum shear slip takes place at the center of the reservoir layer with maximum RSD 0.26 m developed at pore pressure is 50 Bar which is consistent with results reported in [7] (can be seen in figure A.1).

4.3.3. 215 m fault shift

In this case, the reservoir offset is equal to reservoir thickness that is 215 m. The simulated fault behaviours are shown in figure 4.12 and he reference results [7] are shown in appendix figure A.2

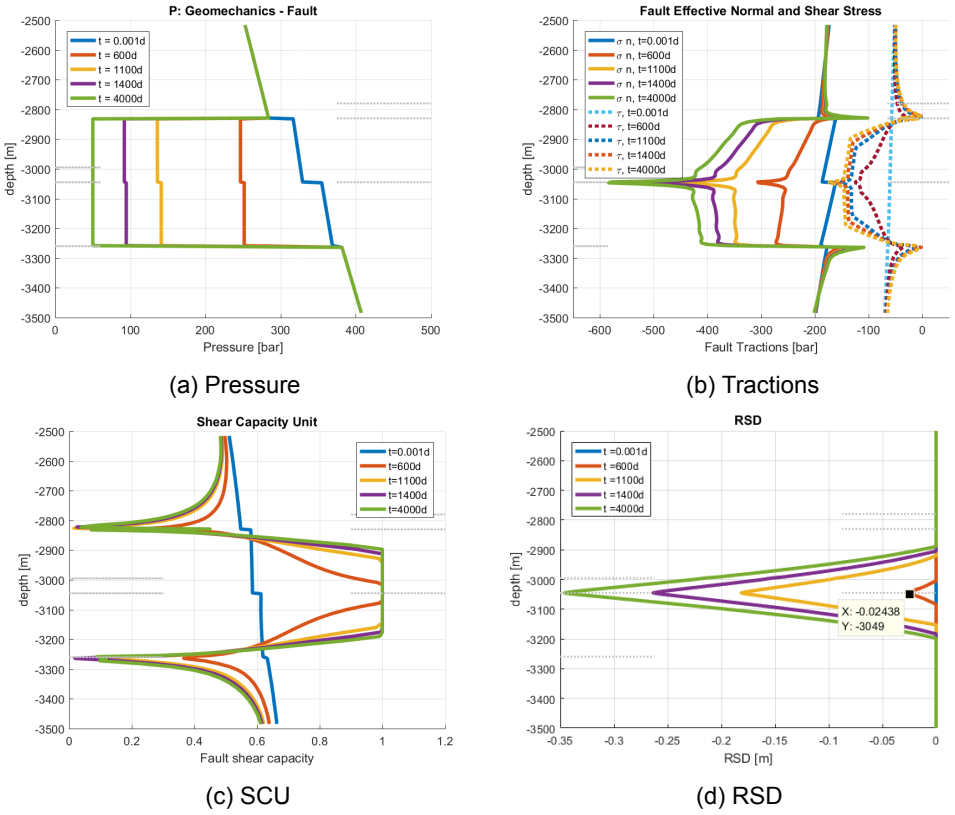

(a) Pressure (b) Tractions

(c) SCU (d) RSD

Figure 4.12: Comparison of ADGPRS simulation results (top) with [7] (bottom).

The pressure distribution in the model is a function of depth. The pore pressure response along the fault in Fig. 4.12a indicates that reservoir layer in the hanging wall (down-thrown) block is

more over-pressured compared to footwall (up-thrown) block, even though the depletion rate is the same for both blocks.

The tractions have the greatest value at depth 3045 mTVD where reservoir bottom boundary of footwall block meets with top reservoir of hanging wall block. The stress concentration along the fault in the reservoir is more severe to induced tractions on fault surface. However, the superposition of effective stresses reaches the maximum at depth 3045 mTVD, as shown in figure 4.13. Therefore, the tractions values are very high at this point and fault starts initiate to fail and rapid development of RSD at that depth.

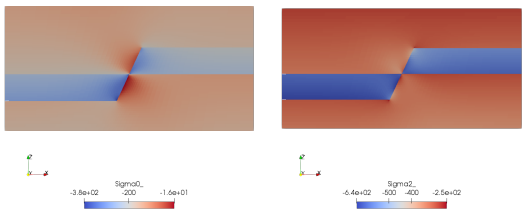

Figure 4.13: 2D effective stress distribution in the block model at final time. $\sigma_x = \sigma_{h_{min}}{}'$ is shown on the left and $\sigma_z = \sigma_V{}'$ on the right

Based on figure 4.12b, tractions are the lowest at the top footwall (2830 mTVD) and bottom hanging wall (3125mTVD) of reservoir layer. Consequently, shear failure is will not likely to occur there (see figure 4.12c), and no RSD observed (fig 4.12c). The failure state of fault can already be observed after 600 days of simulation that corresponds to pore pressure 250 bar and with sliding (RSD) ~ 0.024 m. This supports the fact that fault with a larger vertical throw is more prone to failure which is consistent with a similar conclusion in [7].

4.3.4. 440 m fault shift

The comparison is performed for 440 m offset which is more than twice larger than reservoir thickness. The simulation results are quantified by pressure, tractions, shear capacity utilisation and relative shear displacement and shown in Fig. 4.14, while the reference results[7] can be found in appendix in figure A.3.

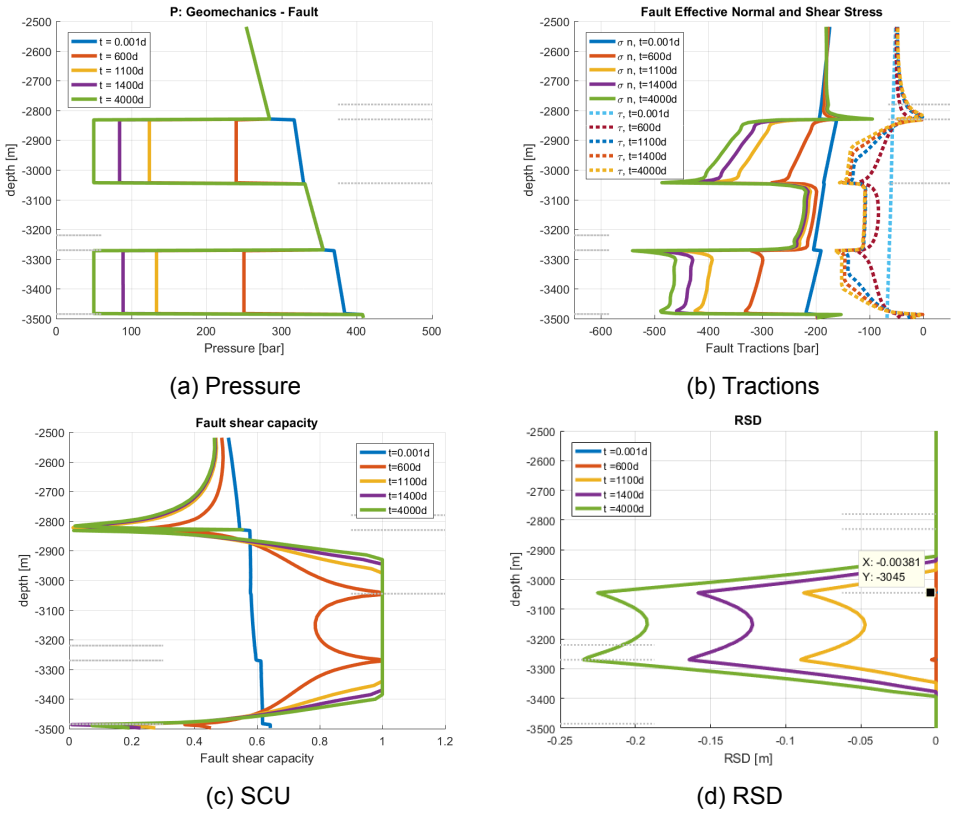

(a) Pressure (b) Tractions

(c) SCU (d) RSD

Figure 4.14: Comparison of ADGPRS simulation results (top) with [7] (bottom).

The pressure response in the figure 4.14a shows again the higher pressure in the foot block. Figure 4.14b describe that fault traction magnitude is minimum at the top and bottom of the footwall and hanging wall block, respectively. Conversely, tractions reach maximum at the base footwall and top hanging wall of reservoir layer. Shear failure is developed at maximal tractions and RSD, as can be seen in fig. 4.14c and fig. 4.14d, and it starts to take place at reservoir pressure 250 bar with RSD is 0.024 m. However, the corresponding RSD value is 0.003m which is less than RSD developed with a lower shift (215 m). Again, these results are in correspondence with reference results [7] as illustrated in figure A.3.

4.4. Discussions

Pressure depletion leads to change of effective stress in the depleting layer (reservoir) and formations around it. The effective lateral stress above and below the reservoir is redistributed which values become greater than the initial effective stress and further induced traction in the pre-existing fault at top and bottom of the reservoir.

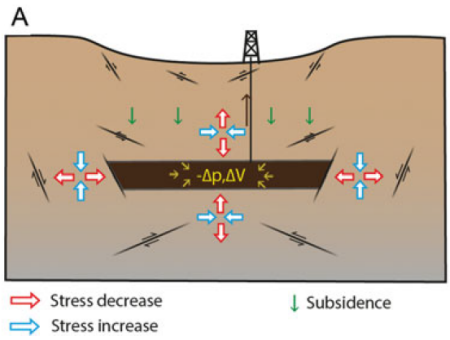

(a) Poro-elastic change in the subsurface [8]

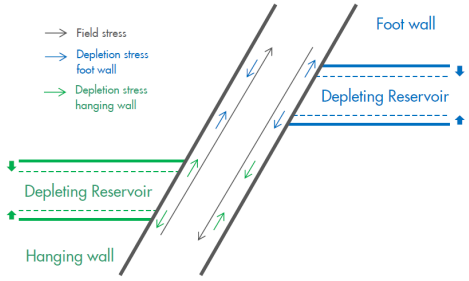

(b) Shear stress exerted on the fault plane in the normal faulting regime[7]

Figure 4.15: The stress field responding to depletion on the formations (left) and fault plane (right). The grey line in fig. 4.15b is shear induced by tectonic.

Figure 4.15b illustrates the total stress field acting on faults surface under a normal faulting regime during reservoir depletion. There are two types of shear working on the fault wall; global shear due to tectonic and local shear as a result of depletion. The local induced shear is positive at the top of the reservoir and negative at the bottom of the reservoir. The layer adjacent to a reservoir that separated by fault, the local stress direction is the opposite from the reservoir wall. However, the global shear in the faulting system are as follows; shear goes downwards on the footwall block and goes upwards on the fault wall of down-thrown block [7]. Shear due to tectonic effect is out of the scope of this project. Regardless the offset fault, shear superposition reaches a maximum at the top and bottom of reservoir respectively in the down-thrown and up-thrown block, whereas, the minimum magnitude is at the bottom and top of hanging wall and footwall block. This explains why top reservoir of hanging wall and bottom reservoir of footwall block always exerts the largest shear, consequently, have the largest shear slip.

Fault slips fastest when the offset is equal to the reservoir thickness. This is because the fault contact area is largest in this configuration. With a small pressure difference ($dP = P_{initial} - P_{final}$) in the subsurface, a larger surface has induced shear and triggered the fault slip. Additionally, the model with vertical shift is more prone to a failure in comparison to model with no offset.

5. The Effects of Production Dynamics on Fault Reactivation

In this chapter, we will perform a sensitivity study of fault reactivation to dynamic regimes of production. In particular, the stress concentration for different production strategies will be analysed. The sensitivity to multiphase flow will be performed by incorporating gas-water contact. The fault response for continuous and discrete production strategy will be compared at the same cumulative gas produced. Discrete production strategy means that there will be a sudden change of production rate by shut-in and re-opened of the well during the production. The sensitivity is executed to conclude whether production strategy affects the fault reactivation.

A similar setup that was validated in the chapter 4 will be used here. The well is placed in the hanging wall block. The major assumption in this study is that fault is defined as conductive with conductivity $C = 1m.Dm$. However, at the beginning of the work, for the same production rate, sensitivity will be performed for two-types of conductivity; non-conductive (sealing fault) with conductivity $C = 1E-12m.Dm$ and conductive (leaking fault). For the leaking fault, the other block is expected to be depleted which flows is passed through the fault plane.

5.1. Comparison between Non-sealing and Sealing Fault

This case will be a simulation with production rate 10,000 m^3/day for both conductive and sealing fault applied in the model with zero offset. The shown results are the responses along the fault that is plotted with respect to time.

The pressure evolution during production along the fault for the sealing and leaking fault cases are illustrated in figure 5.1.

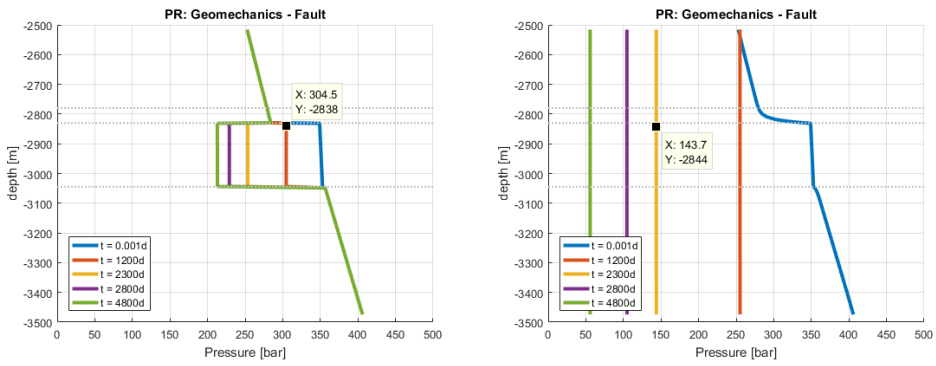

Figure 5.1: Pressure profile for sealing fault (left) and leaking (right) fault

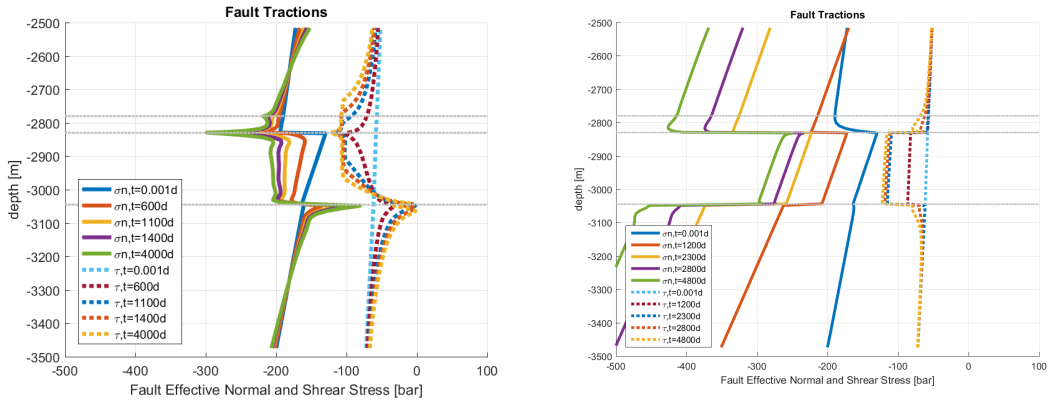

(a) Tractions evolution during production for sealing fault (left) and leaking fault (right)

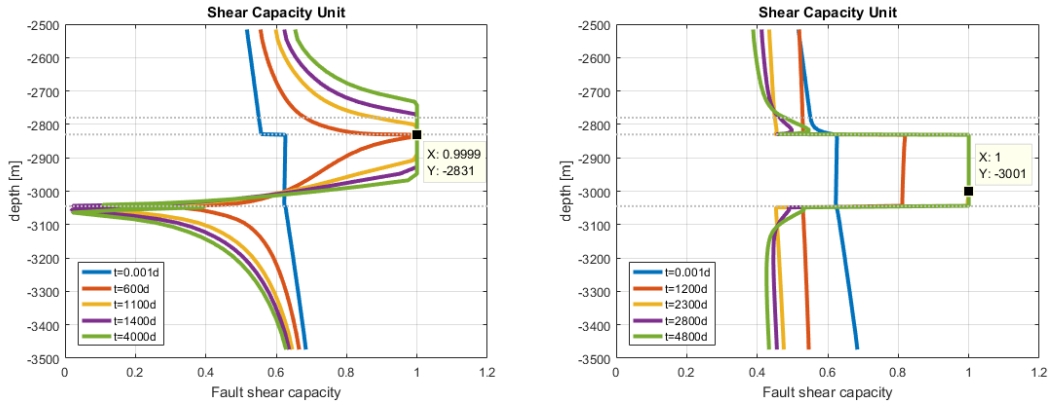

(b) SCU evolution during production for sealing fault (left) and leaking fault (right)

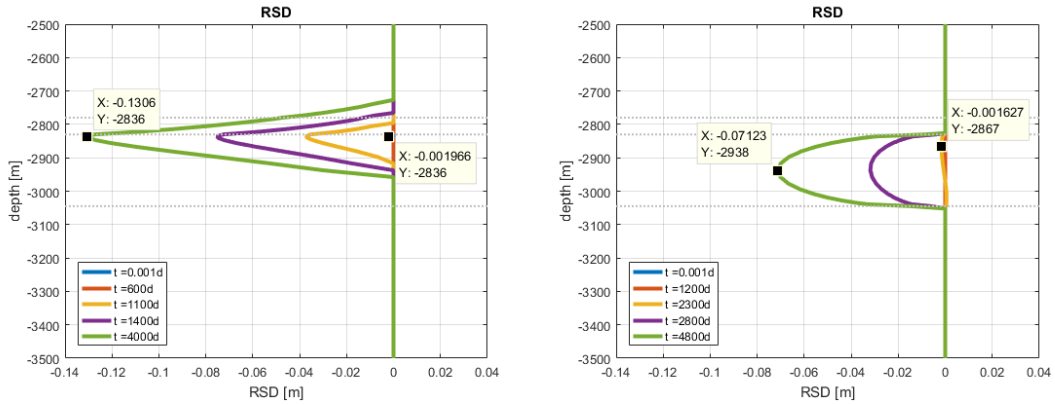

(c) SCU and RSD evolution during production for leaking fault

Figure 5.2: Tractions, SCU and RSD evolution during production for sealing fault (left) and leaking fault (right)

The geomechanics responses along the fault; tractions, SCU, and RSD are depicted in figure 5.2. For the sealing fault case, the fault failure falls (SCU = 1) at pore pressure 300 bar, while for the leaking fault case, fault fails at pore pressure 145 bar. Recall that the well is placed in the hanging wall only. The volume of the reservoir for the sealing case is half of the non-sealing case. Small perturbation on the relatively small volume leads to early failure of the fault. According figure 5.2b on the left side, deformation starts occurring at the top of reservoir and developed around following the large tractions acting on top reservoir fault. The tractions have the lowest values at the base of hanging wall and consequently, no deformation is being observed. For the leaking fault case, fault starts slipping at pore pressure around 145 bar (see figure 5.2b on the right side). The reactivation was first seen at the top of hanging wall with slip developed around 0.0016 m. The fault reactivation then propagates downwards. The slip due to deformation is the largest in the center of the reservoir.

5.2. Effect of Flow Rate Variability on Fault Behavior

The flow rate for base case simulation is 10,000 m^3/day. We compare simulation results for this production rate with results obtained for the rate at 5,000 m^3/day and 20,000 m^3/day. The study will be carried out for the four different offset fault; 0 m, 80 m, 215 m and 440 m. It is important to remark that the fault is conductive from this sub-chapter.

For the given production rates, the corresponding simulated bottom hole pressure (BHP) and cumulative production NP for zero offset is depicted in figure 5.3.

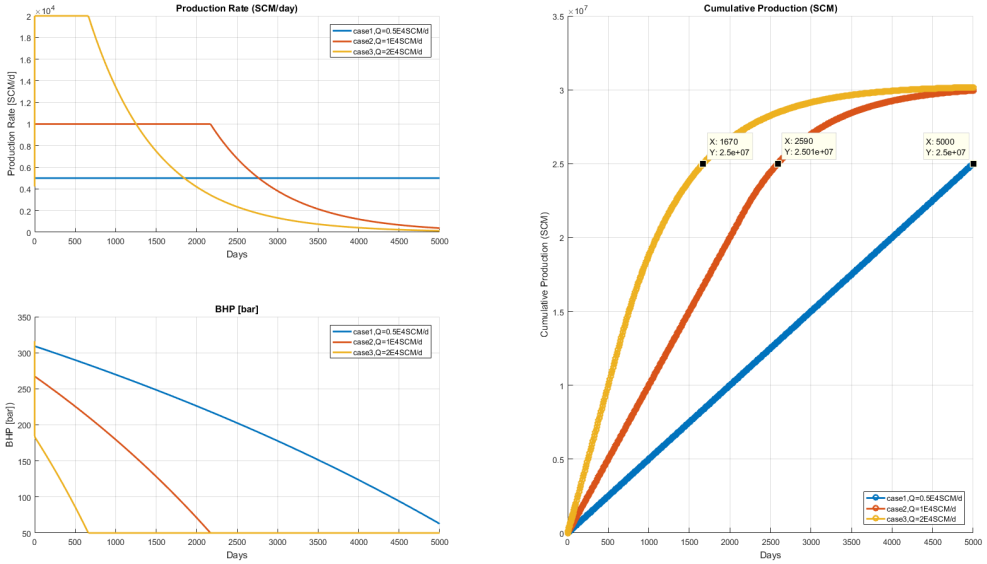

Figure 5.3: BHP and cumulative production NP as results of different rates

Based on figure 5.3, the equal production of 25 million m^3 of gas is reached for all different rates (10,000, 5,000 and 20,000 m^3/day) at 5000, 2590 and 1670 days of simulation, respectively. Note that fault in this simulation is conductive. Although only reservoir layer is depleted, flow occurs along the fault section, and its pressure goes down during the production process, as depicted in figure 5.4.

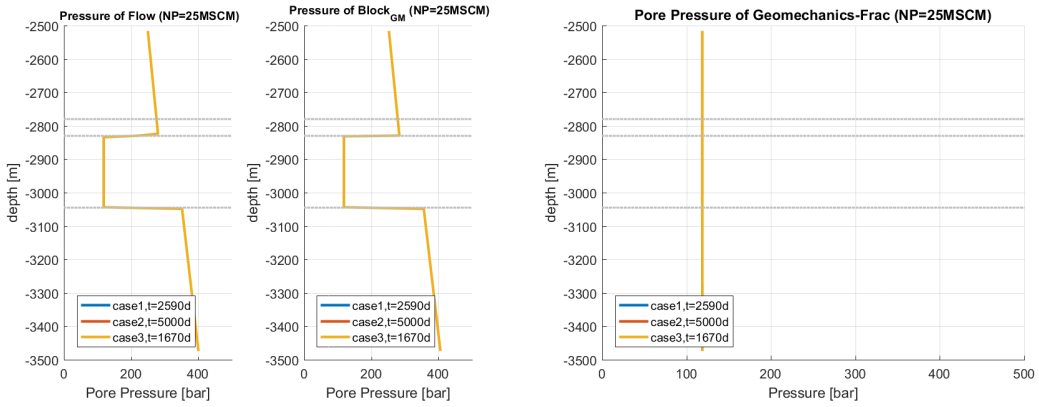

(a) Pressure profile on the block model (b) Pressure profile along the leaking fault surface

Figure 5.4: Figure 5.4a shows the pore pressure on the block model both from flow and geomechanics solution. figure 5.4b is pressure along the fault plane. The fault plane is conductive for accommodating flow through fault. Both are plotted at NP 20 MSCM as results of different rates

For 0 m offset, the corresponding fault behaviour at the same NP 20MSCM produced can be

observed with: tractions, SCU and RSD, that is shown in figure 5.5. The results demonstrate that there is no difference in tractions, SCU and displacement distribution along the fault for all three rates in the study. These observations indicate that the fault slip and corresponding seismic event is not affected by the rate of production and only depends on the volume of production.

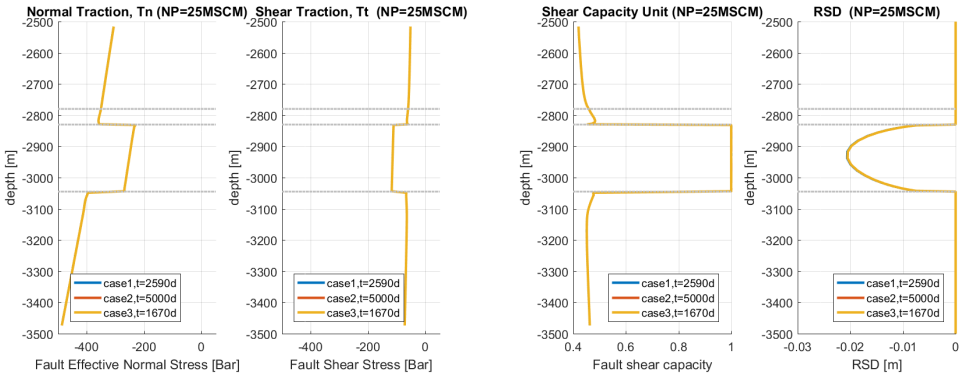

(a) Fault tractions. (b) SCU and the corresponding shear slip.

Figure 5.5: Tractions, SCU and shear slip (RSD) acting on the fault surface at NP 20 MSCM for different production rates

The production profiles (BHP and cumulative gas production NP) for various offset are illustrated in detail in appendix B.1. The effect of varying rates on pressure profile along the fault plotted at the same cumulative gas produced for different offsets are illustrated below.

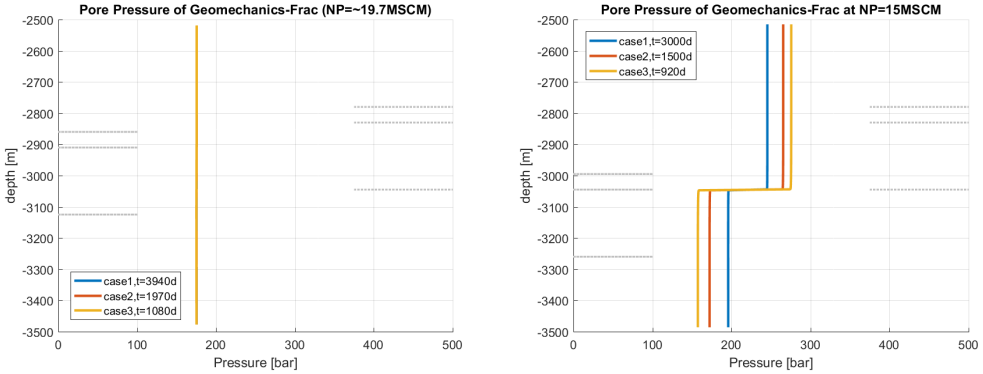

(a) Pressure response along the fault with offset 80m (b) Pressure response along the fault with offset 215m

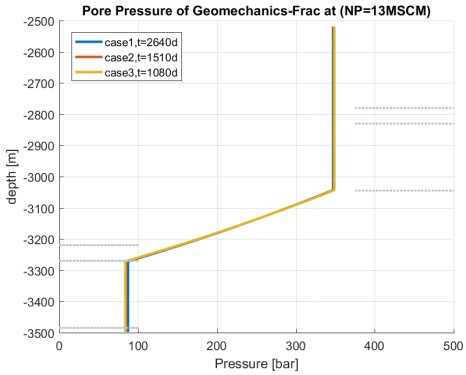

(c) Pressure response along the fault with offset 440m

Figure 5.6: Pressure response along the fault with offset; 80 m; 215 m; 440 m.

The corresponding fault tractions, RSD and SCU for different offset is shown in figure 5.10 below.

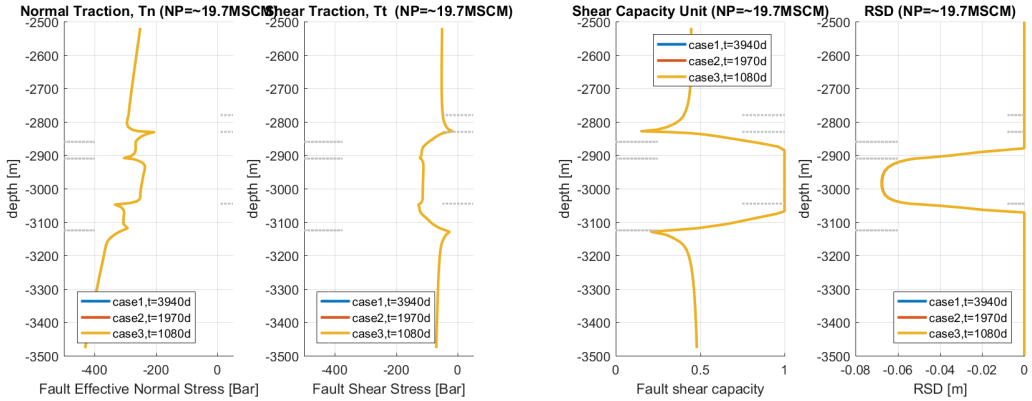

(a) Tractions, SCU and the corresponding shear slip along the fault with 80 m offset.

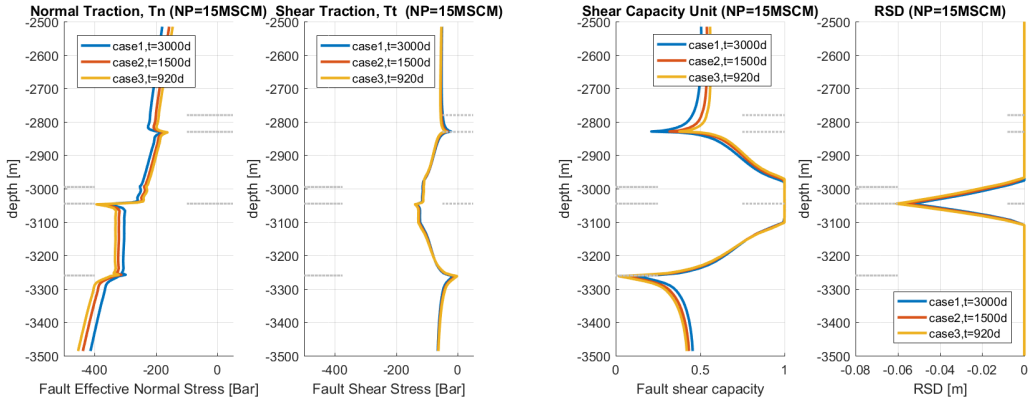

(b) Tractions, SCU and the corresponding shear slip along the fault with 215 m offset.

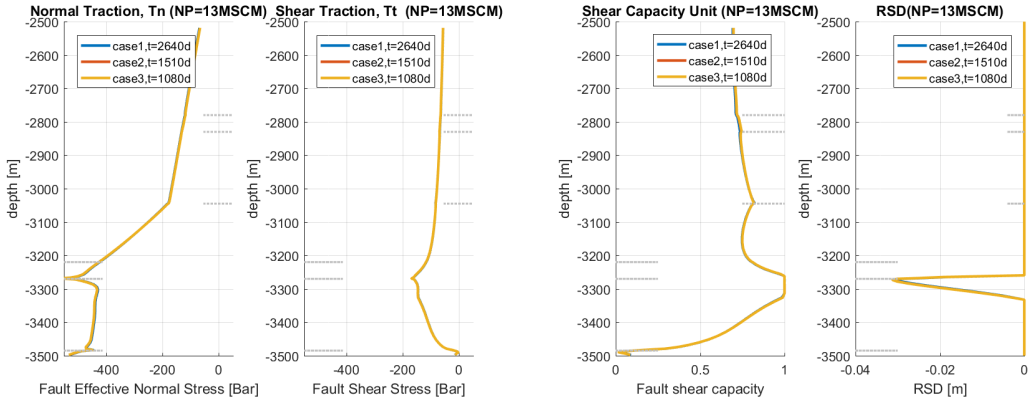

(c) Tractions, SCU and the corresponding shear slip along the fault with 440 m offset.

Figure 5.7: Pressure, tractions, SCU and shear slip (RSD) profiles acting on the fault surface at the same NP for different production rates

When the fault throw is less than half of reservoir thickness which in this case is 80 m, as the hanging wall block is depleted then the footwall block also gets depleted with production rates almost as fast as depletion rates in hanging wall block. Evidence that both block get depleted is shown in the middle of figure 5.6. It can be inferred that pressure between footwall and hanging wall block reaches equilibrium fast. Keeping the observations in the reservoir layer only, the magnitude of high shear present at the top of hanging wall and base of footwall block. Again, the maximum shear slip is developed in the center of reservoir layer.

The model with an offset equal to reservoir thickness (figure 5.17a), the variability of production

rates changes the stress state distribution as well as other mechanics properties along the fault. As the production well is placed in the hanging wall block, the footwall block is being depleted by flow through fault. In the case of high depletion rate, the down-thrown block is depleted faster than the other block because flow through the matrix has bigger contribution than the flow through the fault, resulting in slower depletion rate in the up-thrown wall block. Conversely, in the case of the lower rate, flow through fault is quite prominent such that hanging wall and footwall block are being depleted almost at the same rate even tough the well is only located in the hanging wall block. In general, a varying rate that has different pressure response would also develop different stress state and the other geomechanics state in the subsurface accordingly. However, this is only valid when the offset is equal to reservoir thickness.

In the case where formation offset is more than twice of reservoir thickness, that is 440 m, as the hanging wall block is producing, the footwall block is depleted very slowly and can be seen as almost not depleting. This is because the reservoir offset is too large (twice as reservoir thickness) and the production of non-depleting block is strongly affected by fault conductivity. From the pressure profile, there is a slight pressure discrepancy along the fault in contact with the two reservoir blocks. The discrepancies become more pronounce if the rate variability is more vary (see appendix, figure B.4). The top of hanging wall has high production-induced shear while the bottom of footwall block does not and this explains that reservoir in the footwall block is not producing. The fault is not conductive enough to accommodate depletion from footwall to hanging wall block.

5.2.1. Effect of flow rate to slipping dynamics

Next, we study the effect of production rates to the number of fault elements that slipped at the initial stage. A new model is developed to observe phenomena. The model has a low compressibility of gas and water, with the pvt data is shown in Table 5.1 and simulated using the zero-offset model.

Table 5.1: New PVT input parameters to investigate effect of low and high rate case on the failing elements

Water Properties	**Compressibility [bar-1]**	1.00E-07
Gas Properties	**Bg at P = 1000bar**	0.9
Production rate	**Low rate case [m^3/day]**	5,000
	High rate case [m^3/day]	40,000

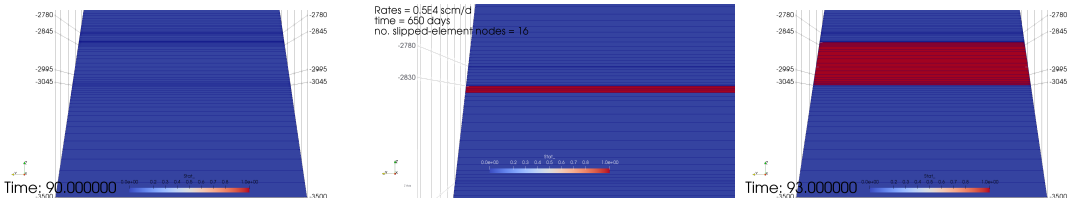

(a) Fault mechanics for low production rate

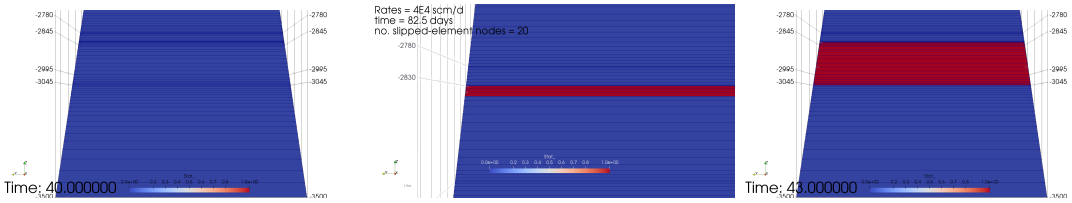

(b) Fault mechanics for high production rate

Figure 5.8: Fault mechanics status when failure starts to develop for the case of low rates (top figures) and high rates (bottom figures). Elements in red is already reaching failure

Our results demonstrate at the initial stage of failure development, for a higher rate (40,000 m^3) a larger scope of area reaches failure than at the lower rate (5,000 m^3). In other words, a greater number of elements fails when depletion rate is higher. This is because the fast flow

rate forces the stress field to develop faster and induce a greater area exposed to the failure. This means that while the time of the seismic event is not sensitive to the production rate, the amplitude of the event is affected since it is proportional to the area of failure.

The simulation results are shown in figure 5.8. The figure on the left is the fault mechanic status before slip is taken place. The blue color indicates that all elements are in stick condition. In the right figure, the mechanic status at the next timestep, corresponding the same commutative production rate, is shown for the low-rate (top-right figure) and high-rate simulation (bottom-right case). For the low production rate, the number of slipped elements is 16 when for the high production rate, 20 elements slipped. Notice that for both examples, failure starts at the top of the reservoir then propagates downwards and only elements contacting reservoir layer are slipped in this case. The right figure shows later time when the part of the fault, contacting reservoir layer, fully slipped.

An in-depth look at the cumulative production (NP) of high rate and low rate case when the failure starts to develop, as is illustrated in figure 5.9, shows that the NP at which fault fails will differ for different production rate. For the high rate case failure takes place at NP 3.272Mm^3 with fault pressure 71.37 Bar and become fully developed at NP 3.39Mm^3 with fault pressure 60.55 Bar. Likewise, for the low rate case, fault failure takes place at NP 3.28Mm^3, fault pressure 70.24 Bar and fully developed at NP 3.375Mm^3, fault pressure 62.14 Bar.

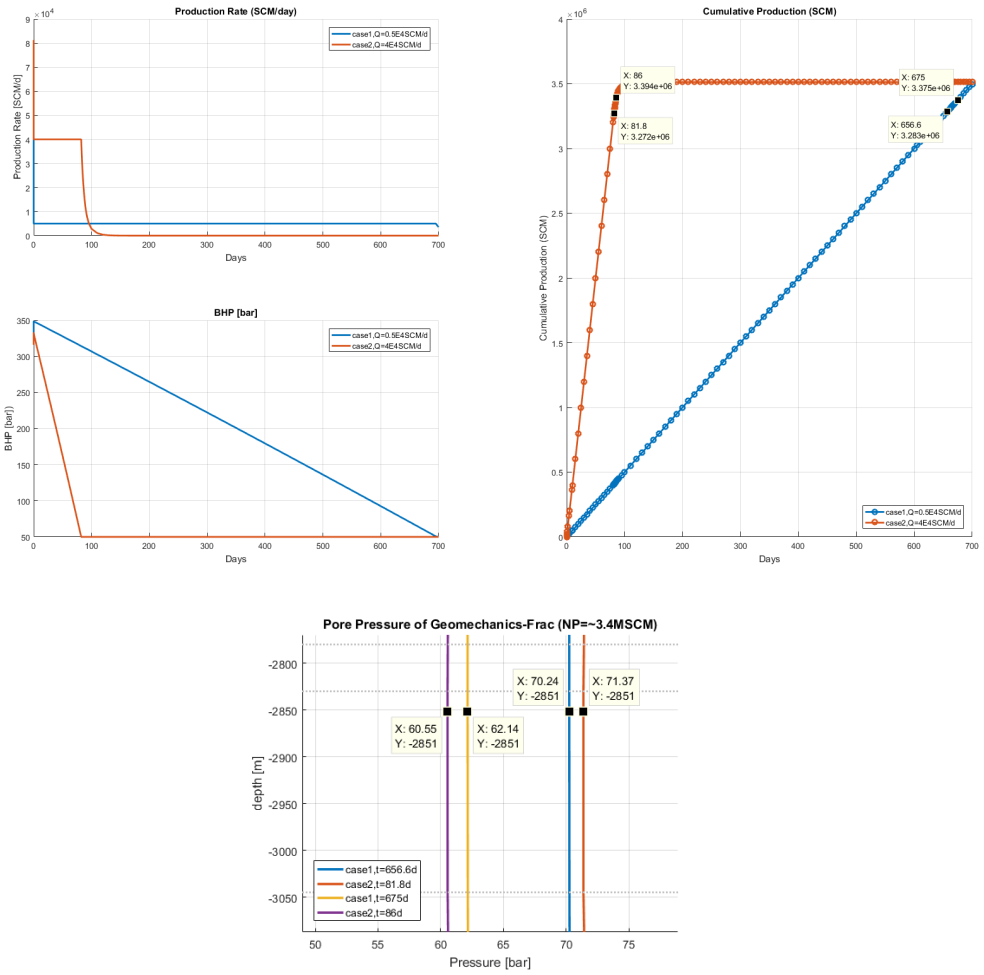

Figure 5.9: Production profiles (top) and pressure profiles (bottom) along the fault when failure takes place and fully developed along the fault intersecting reservoir layer.

5.3. Effect of Multiphase Flow on Fault Stability

In this part of the study, gas water contact (GWC) is being introduced at 2995 mTVD and reservoir above GWC was filled with gas and residual water. The rest of the formations is assumed to be filled with only water. The fault is defined as conductive in which fluid flow can occur along the fault. The fault behaviour with respect to the production dynamics during continuous and delayed production is observed. Continuous means that production is performed at a constant rate during the simulation time. The delayed production corresponds to the shut-in operation during the simulation. The comparison for both cases will be carried out at the same cumulative gas produced (NP).

The continuous production is simulated with rate 10,000 m^3/day. For the delayed production case, the simulation sequence is as following; 30 days of simulation, 30 days of well shut in, and then well will be open for the rest of production life. Keeping observation at the same NP produced, the geomechanical response will be observed, whether or not the stress concentration in the subsurface changed due to delay. The production profile; rate, BHP and NP produced can be found in appendix B.1 as well as pressure and saturation profile on the block model. The pressure and saturation response along the leaking fault are owing to continuous and delayed production that is plotted for NP produced of 20 M m^3/day is illustrated below.

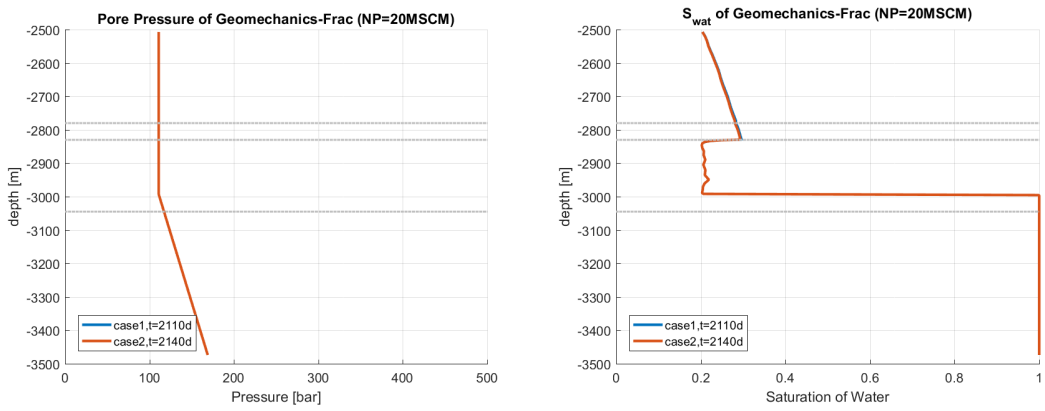

(a) Pressure and saturation responses along the fault with zero offset.

Figure 5.10: Pressure and saturation profiles along the leaking fault with zero offset at 20 SMCM of NP produced for both continuous and delayed production

Recall that in the initial condition, mobile gas fills the reservoir layer above GWC and water fills the rest of the domain. According to the saturation profile, gas moves to the top section of the fault because gas has low-density property and gas-water mixture is created in the upper section of the fault with heavier density remains in the lower part. Based on the pressure profile above, it can be inferred that gas column is depleted faster than water column since gas has high compressibility. This is seen by the pressure in the reservoir layer, above GWC already reach around 105 bar while below GWC is slightly higher.

The tractions, failure criterion and shear slip profile along the fault is depicted of both continuous and delayed production case plotted at the NP produced in figure 5.11. It is observed that there is no difference in stress concentration due to delayed production, consequently, the fault shear capacity and shear slip profile is also the same for both cases.

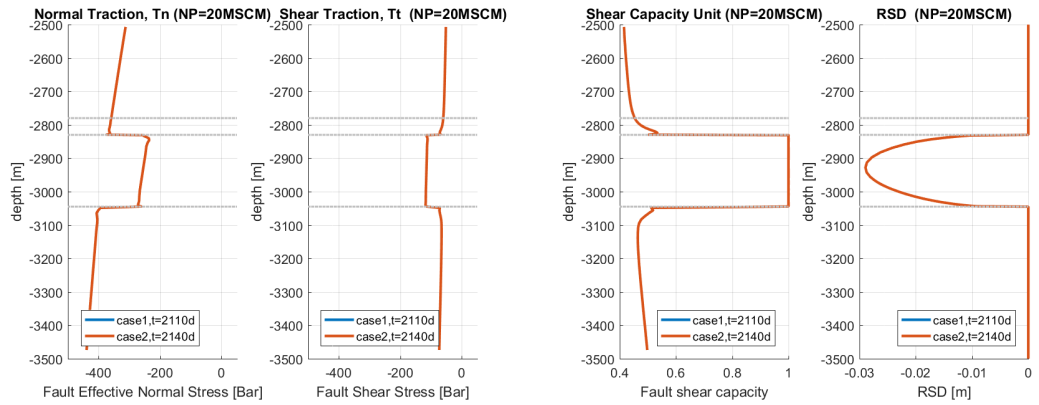

(a) Fault tractions, SCU and the corresponding shear slip.

Figure 5.11: Tractions, SCU and shear slip (RSD) acting on the fault surface at NP 20 MSCM for different production rates

The same strategy is applied to models with different layers offset. The pressure and saturation profiles along the fault plotted at the same NP produced for each offset are depicted in the appendix. Based on the figures, at the same NP produced, the continuous and delayed production (well shut-in and reopen) does not change the stress field in the subsurface.

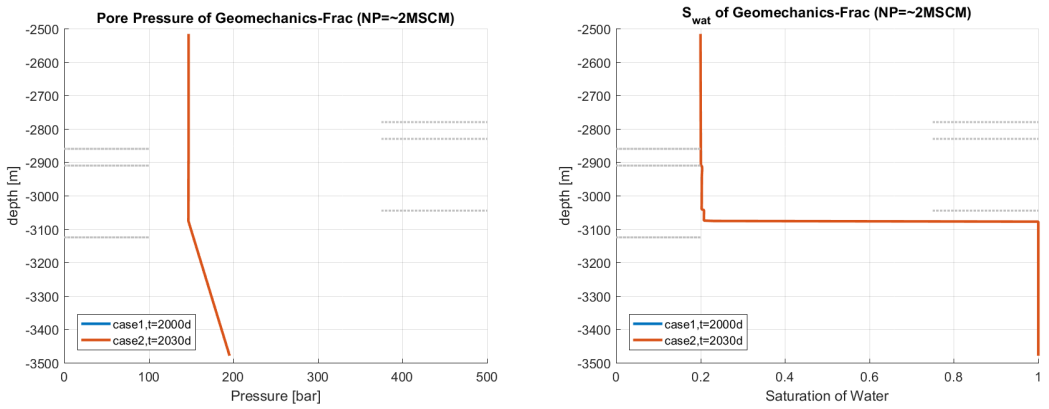

(a) Pressure and saturation responses along the fault with 80 m offset.

Figure 5.12: Pressure, tractions, SCU and shear slip (RSD) profiles acting on the fault surface at the same NP for different production rates with 80 m offset.

The pressure and saturation profiles at the same cumulative gas produced for different offsets are illustrated in figure 5.14. The pressure and saturation profiles have the same trend for continuous and delayed production case. As the depletion is simulated in the hanging wall block, the corresponding pressure drop can be seen in the reservoir interval accordingly.in models with larger reservoir offset due to fault, pressure difference become more prominent along the fault between reservoir layers in the hanging wall block and foot wall block. As the fault is defined as conductive, the footwall block is slightly depleted through the fault. However, the depletion rate in the footwall block become lower as the reservoir offset become larger.

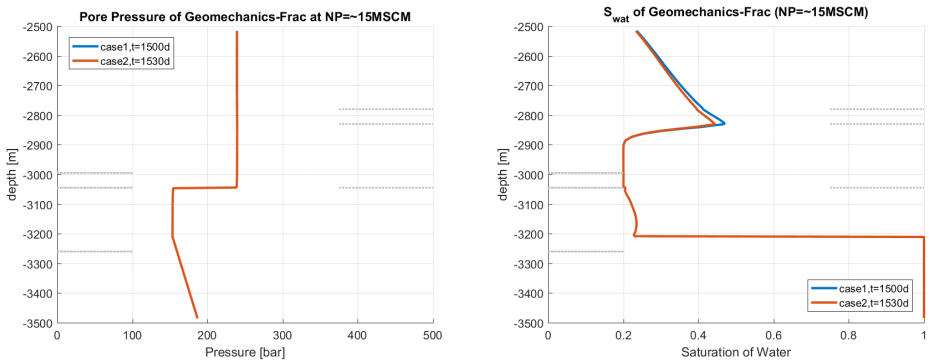

(a) Pressure and saturation responses along the fault with 215 m offset.

Figure 5.13: Pressure, tractions, SCU and shear slip (RSD) profiles acting on the fault surface at the same NP for different production rates with 215 m offset.

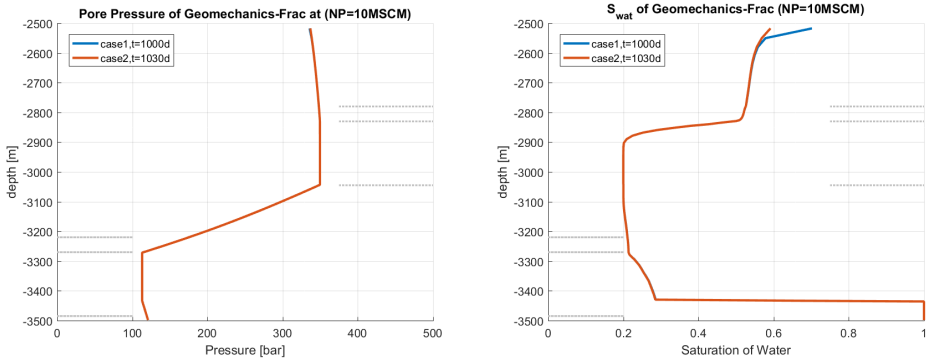

(a) Pressure and saturation responses along the fault with 440 m offset.

Figure 5.14: Pressure, tractions, SCU and shear slip (RSD) profiles acting on the fault surface at the same NP for different production rates 440 m offset.

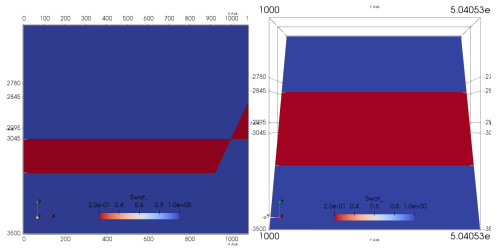

(a) Saturation profile at the initial time in the block model (left) and along the fault surface (right)

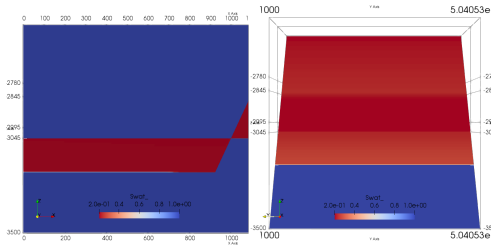

(b) Saturation profile at the initial time in the block model (left) and along the fault surface (right)

Figure 5.15: Saturation profile in the block model (left) and along the fault (right) at the initial time (top) and final time (bottom) for offset of 215 m.

The saturation profile shows that below the gas water contact (GWC) has water saturation $S_w = 1$. However, if a closer look is taken, saturation profile along the fault is curving from

GWC until the top of reservoir layer in hanging wall block. This is because as the gas is produced in the hanging wall, the water starts flowing to the hanging wall block. Figure 5.13a shows that gas saturation builds up near the top of the footwall block during the well shut-in. However, the saturation difference is between continuous and delayed production near the top of footwall block is relatively small that the pressure profile is the same for the two cases.

Figure 5.15 shows the saturation in 2D for the block model (left) and the fault surface (right). Gas saturation is color-coded in red and blue for water. At the initial time, gas is filled in the reservoir of hanging wall and footwall block. The fault surface is saturated with gas in the reservoir interval and water in other layers. At the final time, gas saturation in the hanging wall block decreases as the gas is produced and water starts saturating in the hanging wall. Footwall block is not depleted and gas flows to the top of fault since the gas density is lighter than water.

The tractions, shear capacity and shear slip for continuous and delayed production for different offsets are illustrated in figure 5.18. They are plotted at the same cumulative gas produced; 20 million m^3, 15 million m^3 and 10 million m^3 for offset 80 m, 215 m and 440 m respectively. According to the figure, shear slip occurs when the magnitude of tractions are the largest, that is at the top of hanging wall and base of footwall of the reservoir layer. Based on the geomechanics state of the fault, it can be inferred that delaying production does not change the stress state and deformation.

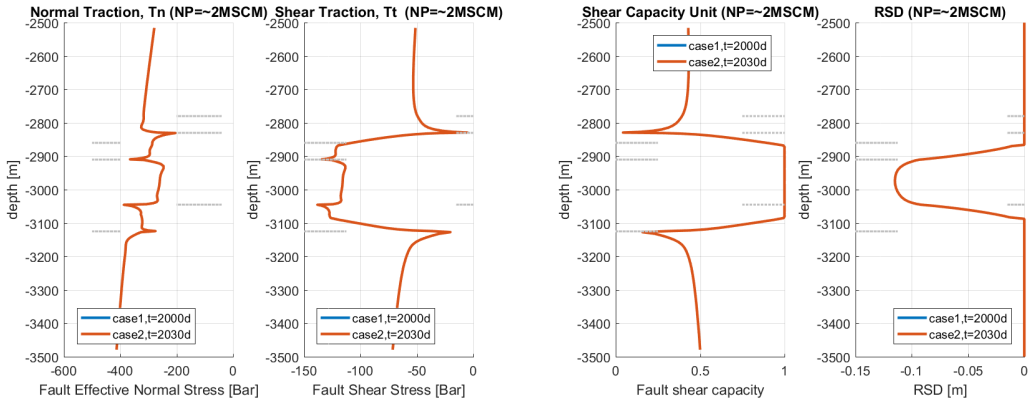

(a) Tractions, SCU and the corresponding shear slip along the fault with 80 m offset.

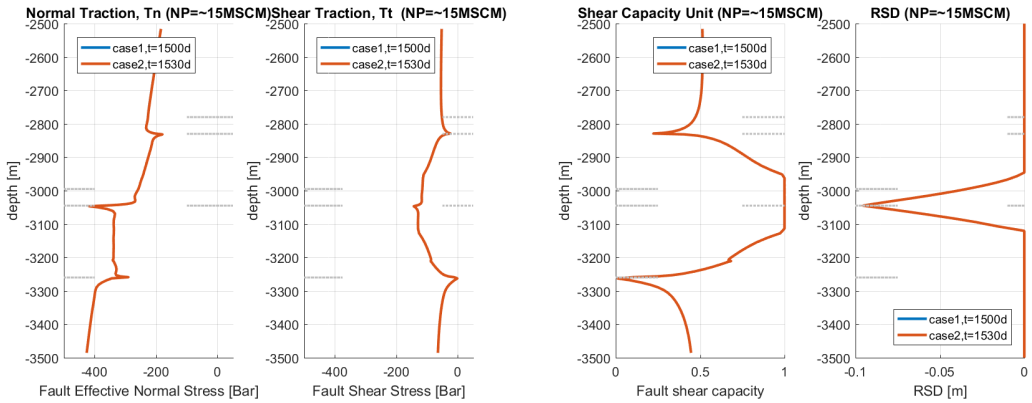

(a) Tractions, SCU and the corresponding shear slip along the fault with 215 m offset.

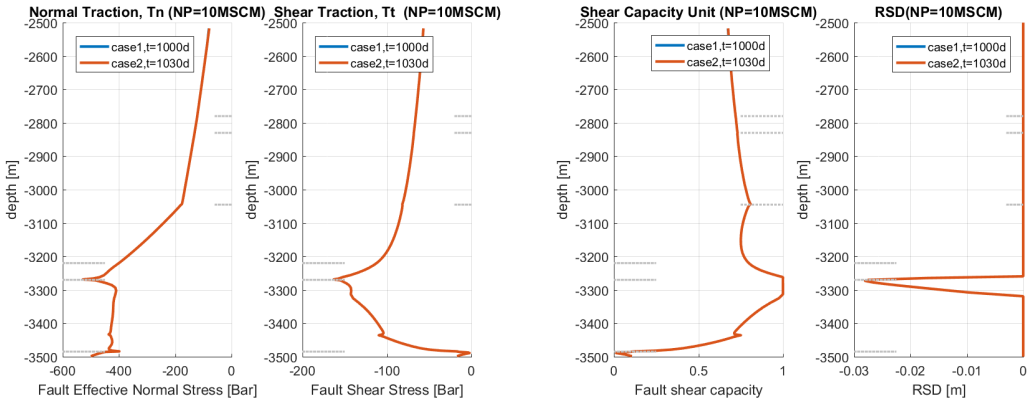

(a) Tractions, SCU and the corresponding shear slip along the fault with 440 m offset.

Figure 5.18: Tractions, SCU and shear slip (RSD) profiles acting on the fault surface at the same NP for different production rates

5.4. Discussions

In this chapter, the sensitivity studies of fault behaviour owing to variability of conductivity, flow rates as well as continuous and delayed production have been carried out. Sealing and non sealing properties of fault determine the reservoir volume as well as the recoverable gas reserves. For both non-conductive and leaking faults, the slip patch is initiated at the top of the reservoir. For the sealing fault, the slip propagates from the top of reservoir to the surrounding formations in which the amplitude of shear slip is the largest. For the leaking fault, slip patch develops the largest amplitude in the centre of reservoir.

When depletion is only located on one side of block separated by fault, the other block can be depleted through the fault. Fluid flow through the fault is allowed when the fault is conductive. Variability of the flow rate might change the geomechanics states and depends on the offset. For a small offset, the fault becomes more conductive when fault surface is reaching failure (see equation 2.35). This will enhance production on the other non-producing block and can be inferred that the depletion of both blocks is nearly uniform. Therefore, the geomechanics state in the subsurface is the same for the different producing rate. For larger offset, non-producing block only gets depleted through the leaking fault. Thus, fault conductivity plays a role in depleting the footwall block since the well is placed only in the hanging wall block. However, the variability of the production rates will vary the geomechanics state in the subsurface and along the fault.

Variability of flow rate plays a role in failure element along the fault. Based on figure 5.9, it can be concluded that the high rate case fails with slightly less NP consequently higher fault pressure in comparison with the low rate case both of which located at the top reservoir. However, the failure fully developed along the fault intersecting reservoir layer where the high rate occurs at slightly greater NP consequently less fault pressure compared to the low rate case.

Continuous and delayed production, where the well is shut in for 30 days during production, were simulated in the model. Comparing results of the schemes at the same cumulative gas produced, it can be inferred that the geomechanics state does not differ due to delayed production. However, it is possible that the fault becomes reactivated during well shut-in if the fault is critically stressed due to production [34]. In the current setup, we cannot reproduce this behaviour and leave it for future research.

6. Case Study

Based on the sensitivity studies in the previous chapter, some conclusions can be drawn. However, the utilized model has an idealistic representation of real properties of Groningen gas field. In this chapter, more accurate model will be developed and simulated.

In this study, the fault is divided into subsections whose properties vary depending on the layering. The geometry of the model as well as the parameters is adopted from [8] which are described in fig 6.1 and table 6.1. Fault surface is not instersecting the Zechstein formation, except the case with fault offset. The fault is only conductive in the reservoir layer for 0 m offset model as well as reservoir juxtaposed with reservoir layer for 80 m offset. This assumption is based on consideration of shale smear that does not allow flow to occur through the fault.

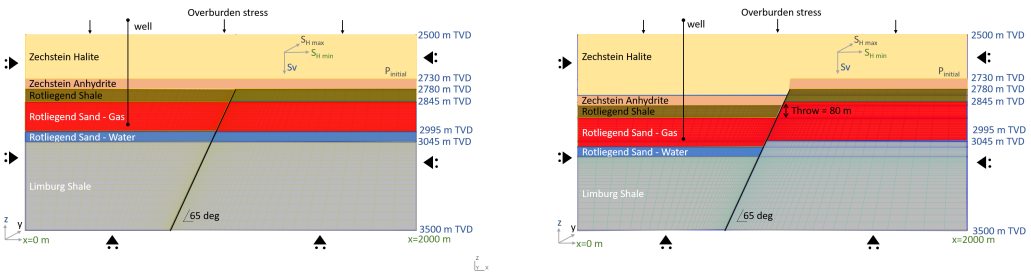

Figure 6.1: Geometry for the case study with 0 m offset (left) and 80 m offset (right). Adopted from[8].

Table 6.1: Parameters for the case study model, adopted from[8]

Formation		ZEZ2H Halite	ZEZ Anhydrate Carbonate	ROCL Ten Boer	ROSL Slochteren	DC Limburg
Rock Properties	Top Depth [m]	-2500	-2730	-2780	-2845	-3045
	Base Depth [m]	-2730	-2780	-2845	-3045	-3500
	Thickness [m]	230	50	65	200	455
	Young Modulus [GPa]	35	65	20	15	25
	Poisson Ratio	0.35	0.3	0.1	0.1	0.2
	Density[kg/m3]	2150	2900	2500	2500	2700
	SH_{max}/Sv	0.795				
	Sh_{min}/Sv	0.72				
Fault Properties	Cohesion [Bar]	30		10	30	30
	Static friction coef. μ_s	0.7		0.4	0.6	0.5
	Conductivity [m.mD]	1E-12			1	1E-12

Gas is filling both ROCL and ROSL formation with gradient calculated in 4.5. Moreover, gas water contact is introduced at 2995 m TVD and 3075 m TVD for 0 m and 80 offset case, respectively. The production well is located in the reservoir layer. The model is run for 4000

days with two production schemes: (i) continuous production, (ii) production was stopped for 30 days after the first 30 days of production which is repeated three times every 1000 days.

6.1. Continuous production strategy

The pressure and saturation profiles along the fault plane for the continuous production strategy with offset configuration 0 m and 80 m are illustrated below

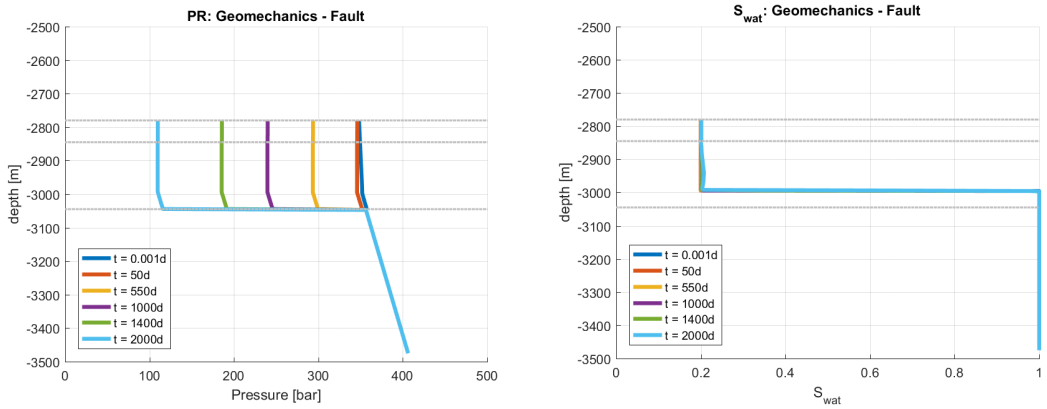

(a) Pressure and Saturation evolution with time for 0 m offset

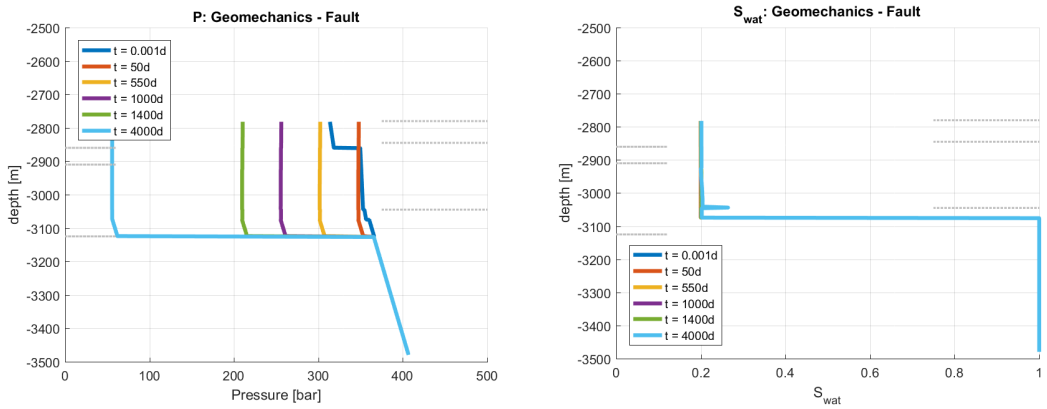

(b) Pressure and Saturation evolution with time for 80 m offset

Figure 6.2: Pressure and saturation profiles along the fault plane of continuous production case for the offset case of 0 m (top) and 80 m (bottom).

The pressure profile at initial time step is in accordance with the initial condition, that is gas fills ROCL and ROSL formation. However, for 80 m offset case, there is a jump of pressure at depth 2845 m TVD due to averaging of pressure at the beginning of the simulation because the conductive fault is only defined for reservoir juxtaposed with reservoir layer. The pressure evolution shows a decrease along the fault during production, due to the fact that fault in non-sealing. The saturation profile along the fault does not change during production.

For 80 m offset, the saturation peak at depth 3045 mTVD appears due to the failure processes. Recall that the fault is more conductive once the fault fail, as fault conductivity is related to gap function (see eq.2.35). The fault elements at this depth failed at the early time and made the element more conductive and water transported in therefore water saturation is locally increased. This phenomena is illustrated in figure 6.3. This effect can not be seen in pressure profile because the pressure behaviour is changing globally while saturation behaviour is changing locally. Note that the fault elements from interval 2780 - 2860 mTVD do not reach failure since the Anhydrite fault properties are defined. In addition to water seeping, it can be inferred that there is no coning effect in this simulation and is probably because aquifer driving force is not strong enough to enhance production.

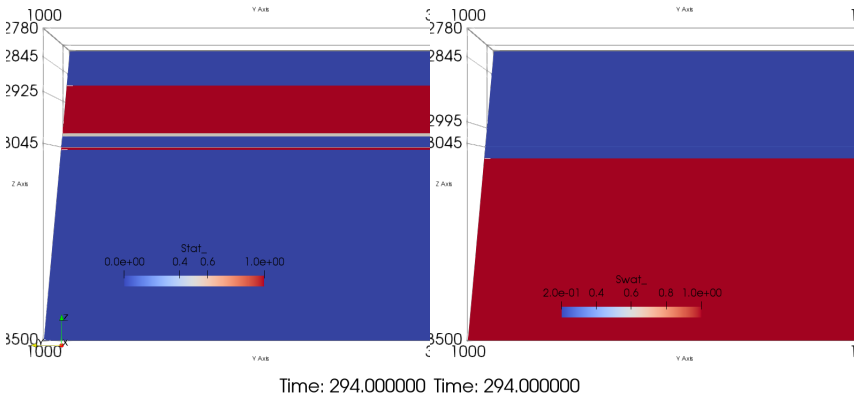

Figure 6.3: Fault mechanics failure status and the corresponding saturation profile along the fault for 80 m offset. It can be seen at depth 3045 mTVD, the reservoir in the base of hanging wall fails consequently saturated with water

The corresponding geomechanics (tractions, shear capacity utilisation and shear slip) evolution along the fault during continuous production case for zero-offset and 80 m offset are respectively seen as in figure 6.4 and figure 6.5.

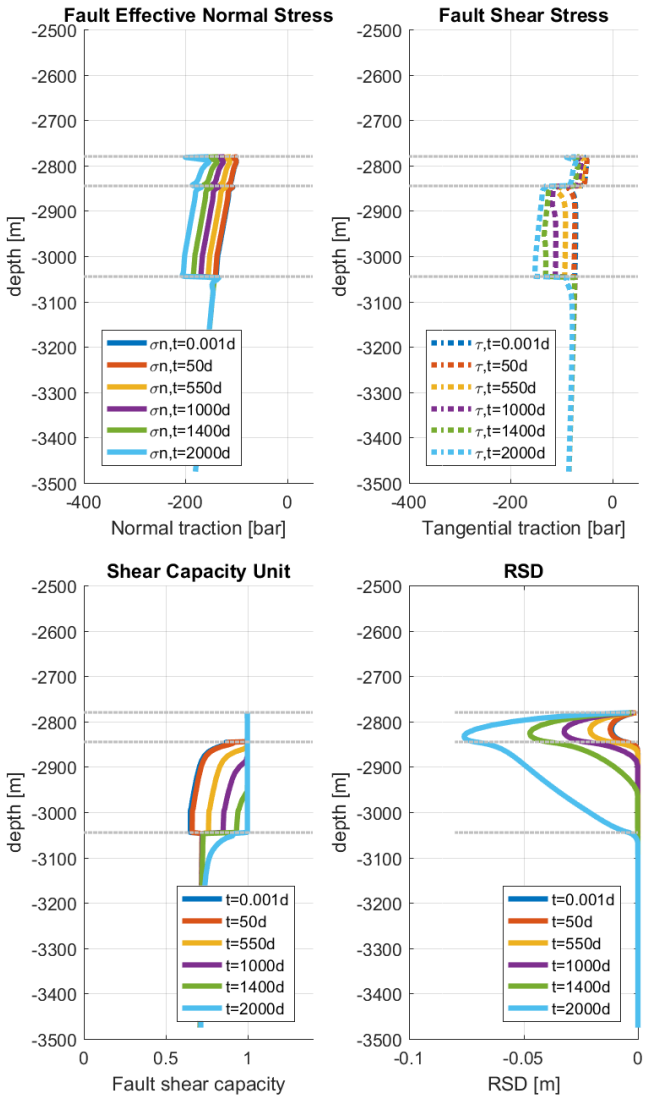

Figure 6.4: Tractions, shear capacity and shear slip evolution during production for 0 m offset

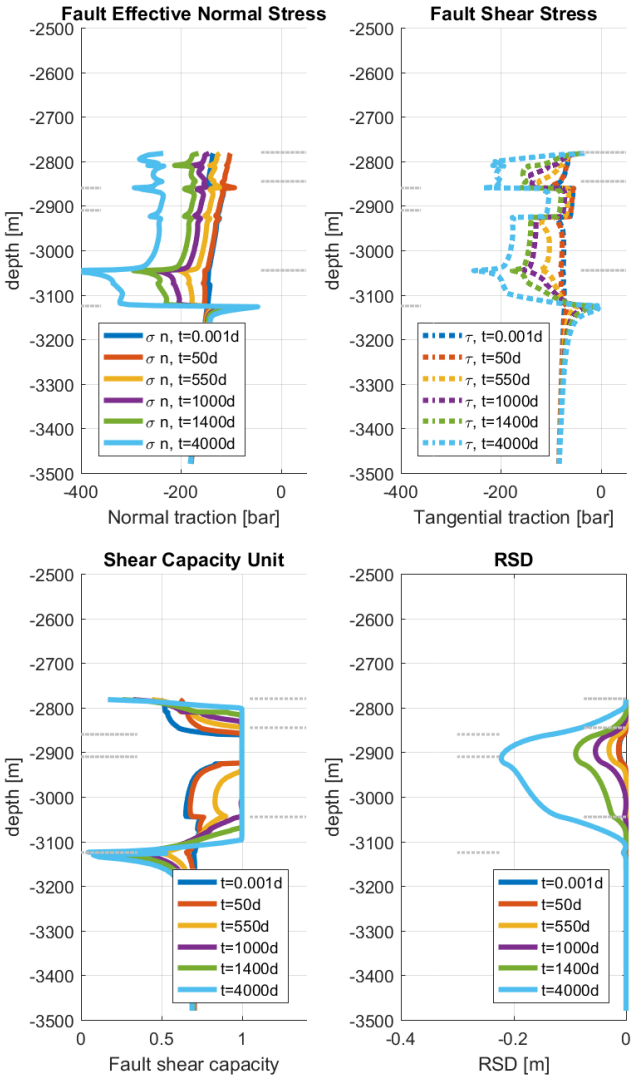

(a) Tractions, shear capacity and shear slip evolution during production for 80 m offset

Figure 6.5: Tractions, shear capacity and shear slip evolution during continuous production case for80 offset case

According to geomechanics response, it can be seen that the shale ROCL layer is already in the failure state at the beginning of the production. It can also be inferred that the shale ROCL is critically stressed even before the start of production. This happens because of the low cohesion and friction parameters defined in the shale layer. Moreover, the heavy and strong salt rock creeps above the shale which makes the fault critically stressed.

It can be seen that the low values of shear in shale formation resulting in failure and deformation (fig. 6.5). Since shale is already at failure condition, the fault in ROCL layer becomes conductive and allow fluid to flow along the fault, as seen in pressure and saturation profile (fig. 6.2). Due to the same reason, deformation owing to production is not only seen in sand ROSL layer but also in shale ROCL even though perturbation is only observed in the reservoir ROSL layer. In general, the failure deveopled with several stages; stage 1, it starts at the top of reservoir ROSL intersecting with shale ROCL layer; stage 2, it then propagates upwards to weak shale ROCL rock; stage 3, it propagates downwards to sand ROSL layer.

6.2. Different production strategies

Now, we compare the results of continuous and delayed production strategy. The observation will be kept at the same cumulative gas produced. The response of the production profiles, rate, BHP, and cumulative gas produced, are depicted in figure 6.6. The blue lines represent continuous production case and the orange lines describe simulation with well shut-in in the middle of production processes.

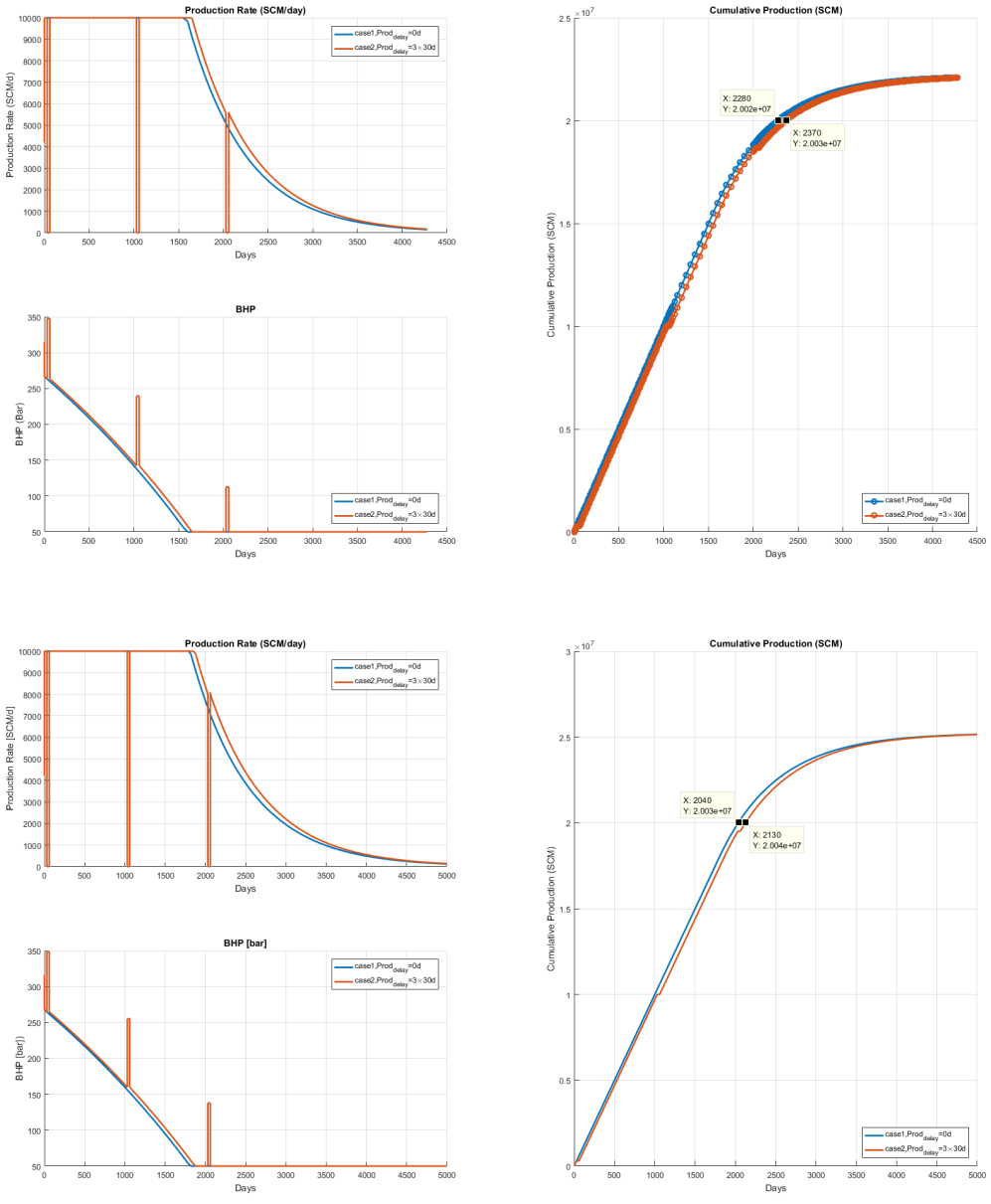

Figure 6.6: Production profiles; rate, BHP and cumulative production for 0 m and 80 offset case

As we simulated the continuous production along with delayed production with a total delayed time of 3×30 days (as seen in figure 6.6, the geomechanics state as the results of continuous and delayed production will be observed with respect to the same cumulative gas produced, in this case is 20 M m^3.

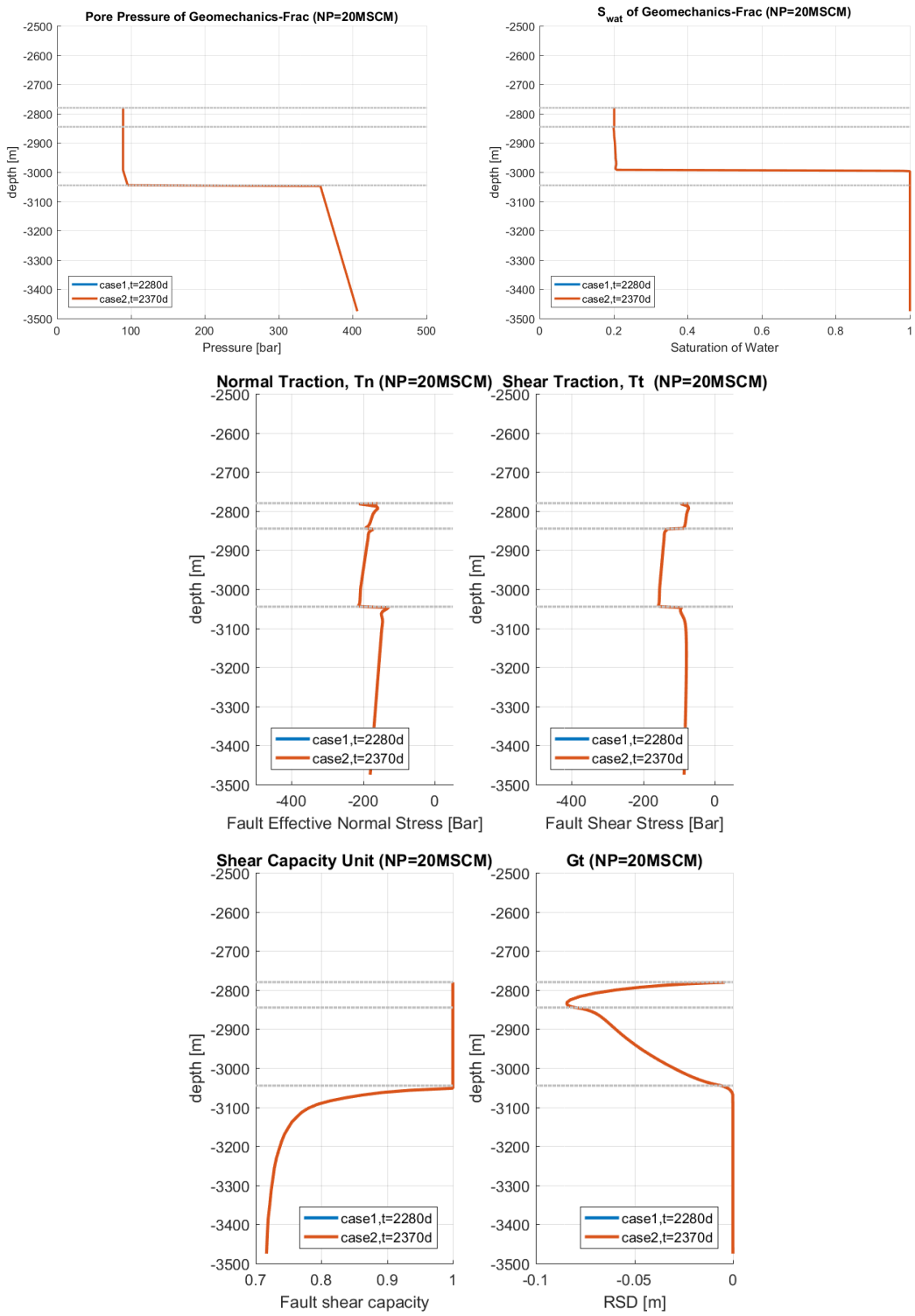

Figure 6.7: Pressure, saturation, tractions, SCU and slip at 20 MSCM cumulative gas produced for 0 m offset

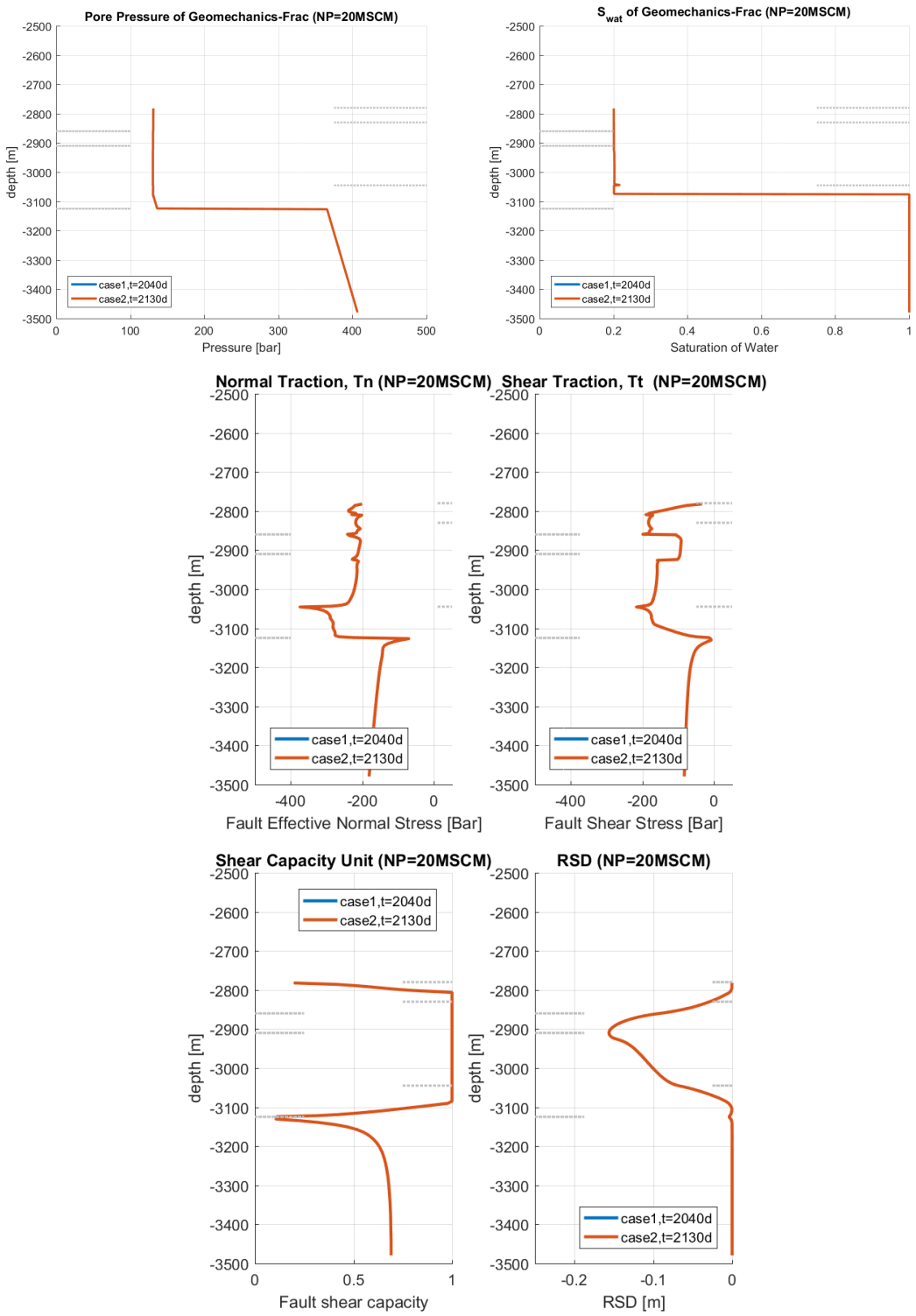

Figure 6.8: Pressure, saturation, tractions, SCU and shear slip at 20 MSCM cumulative gas produced for 80 m offset

Based on figure 6.7 and figure 6.8, it can be concluded that delaying the production does not affect the tractions variations and failure state of the fault in the subsurface in comprison with continuous production vfor zero-offset and 80 m offset. The fault with formation offset has a bigger impact of pressure perturbation that leads to a larger deformation area. The magnitude of shear slip is greater for a larger offset fault.

6.3. Discussions

Weak rocks can be represented by a low static friction coefficient and cohesion. When weak shale plays a role of caprock, its disintegration can be easily achieved once pressure perturbation occurs. For all simulation with no offset, the fault reactivation starts at the top of reservoir layer in the hanging wall block and propagates downwards. Fault reactivation can also propagate upwards if the upper layer is a weak rock. However, for the offset of 80 m, the base of the footwall rock is reactivated earlier than the center of the reservoir. The deformation propagation stops at the base of the reservoir hanging wall, or when the reservoir is juxtaposed with a stronger rock defined with a higher cohesion and friction.

During production, the subsurface is subjected to perturbation. Keeping the observation at the same cumulative gas produced, continuous or delayed production scheme with the same production rate does not impact the geomechanics state of the fault.

7. Conclusions and Recommendations

In this project, the effect of the production dynamics on fault reactivation has been studied. The main contribution of this project is to validate the framework for modeling of induced seismicity tightly coupled with dynamic. There are several conclusions can be drawn from the performed simulations.

1. Friction and cohesion are two important parameters defining the fault strength. Fault slips faster when the friction coefficient is small.
2. With a growing increase in the fault offset, the pressure difference ($dP = P_{initial} - P_{final}$), required to induce shear slip, is decreasing. When fault offset is large, induced shear slip can take place with smaller pressure difference. However, when the offset is really large (more than twice of the reservoir thickness), the induced shear slip occurs at comparatively larger pressure difference.
3. Fault conductivity plays an important role in the dynamic of reservoir response. Production in the hanging wall block can stimulate the footwall block to deplete through the fault depending on its conductivity.
4. The correspondence between flow rates variability and geomechanics state depends on the offset fault configuration. For the same cumulative gas produced, the small offset does not affect stress field in the subsurface. At the same time, the large offset changes the geomechanics state of the fault.
5. In the case of continuous and delayed production, the subsurface stress state does not change when they are compared at the same value of cumulative gas produced.

As the current study only represent fault as a single plane, fault zone with complex structures consisting of a fault core and a damage zone can be developed and assessed. The proposed modelling approach can be applied to heterogeneous reservoirs where the impact of fault reactivation needs to be investigated. Moreover, the elastic response is an idealized assumption any way therefore more work is needed for the future. Considering physics complexity, incorporating poro-thermoelatic to the modeling can also be performed for future work.

A. Model validation

This chapter of appendix is dedicated to show the reference results of the proposed model [**?**]Bogert2015 to be compared with the ADGPRS simulation results. The reference results are grouped into different fault offset; 80 m; 215 m and 440 m.

A.1. 80 m fault offset

The figures below illustrate the pressure, tractions, SCU and RSD of the reference results [7].

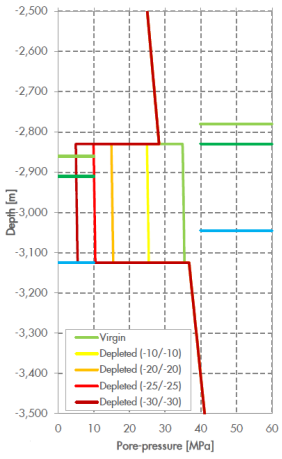

(a) Ref. pressure [7]

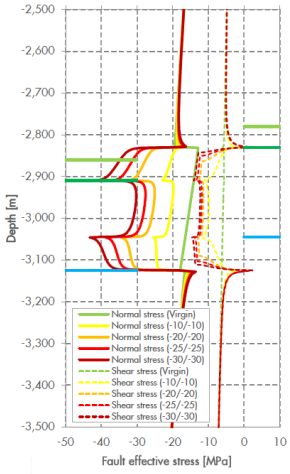

(b) Ref. tractions [7]

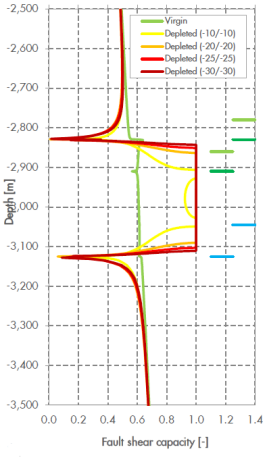

(c) Ref. SCU [7]

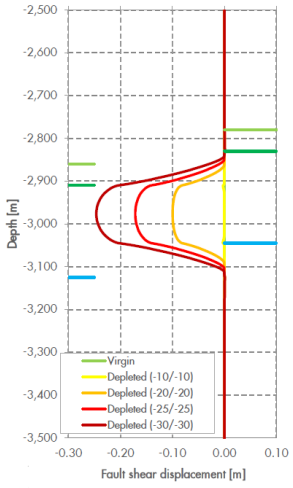

(d) Ref. RSD [7]

Figure A.1: Reference results for 80 m fault offset [7]

A.2. 215 m fault offset

The figures below illustrate the pressure, tractions, SCU and RSD of the reference results [7] for 215 offset.

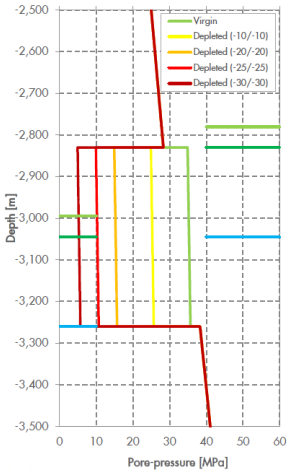

(a) Ref. pressure [7]

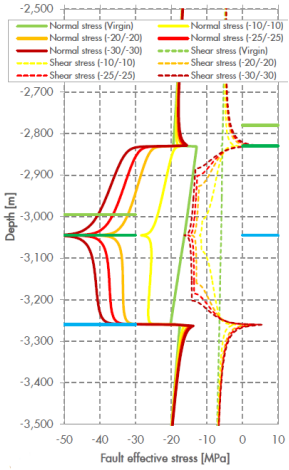

(b) Ref. tractions [7]

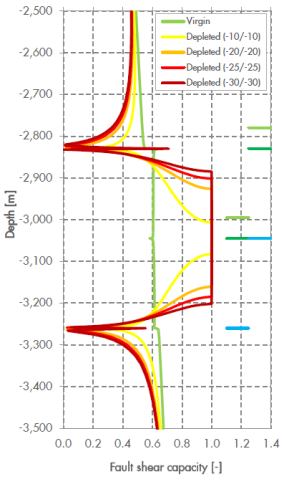

(c) Ref. SCU [7]

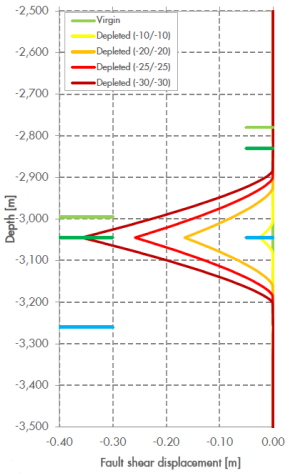

(d) Ref. RSD [7]

Figure A.2: Reference results for 215 m fault offset [7]

A.3. 440 m

The figures below illustrate the pressure, tractions, SCU and RSD of the reference results [7] for 440 offset.

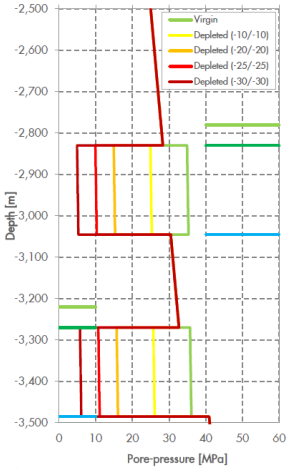

(a) Ref. pressure [7]

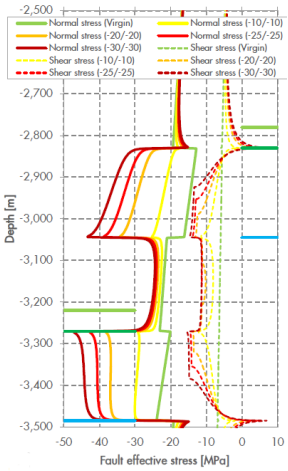

(b) Ref. tractions [7]

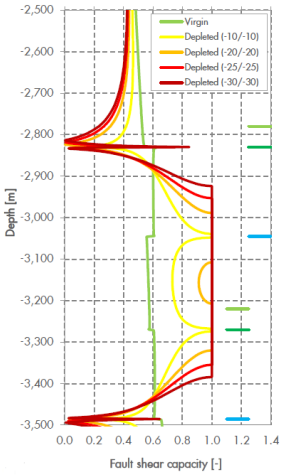

(c) Ref. SCU [7]

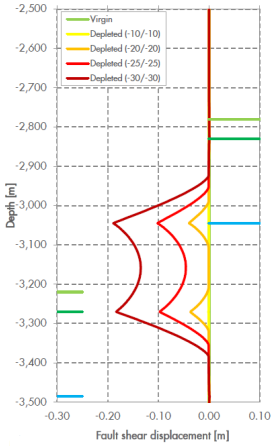

(d) Ref. RSD [7]

Figure A.3: Reference results for 440 m fault offset [7]

B. Production Dynamics on Fault Reactivation

B.1. Variability of flow rate

The production profiles for various rates of each offset are depicted in figure **??**. The observations are; rate, BHP and cumulative gas produced. Based on the figure, larger offset has less cumulative gas produced. The maximum cumulative production for each of the offset are as follows;

1. 80 m. The maximum cumulative gas produced (NP) is reaching 30 million m^3. The cumulative production (NP) that will be used for comparing continuous and delayed production case is 20 million m^3 with days of simulation are respectively 3940 day, 1970 day and 1080 day for low rate (5,000 m^3/day), base case (10,000 m^3/day) and high rate (20,000 m^3/day).

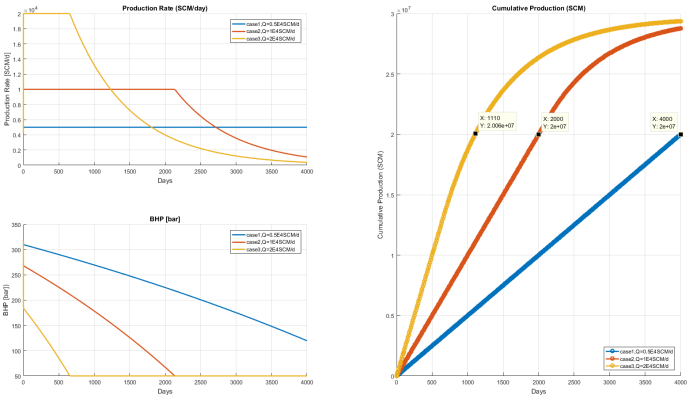

Figure B.1: Production profile; rates, BHP and cumulative production for 80 m offset fault

2. 215 m. The maximum cumulative production is around 27.5 million m^3. The response of various rates will be compared at the same number of cumulative gas produced, that is 15 million m^3. The day of simulation taken for comparing low rate, base case and high rate are 3000 day, 1500 day and 920 day, respectively.

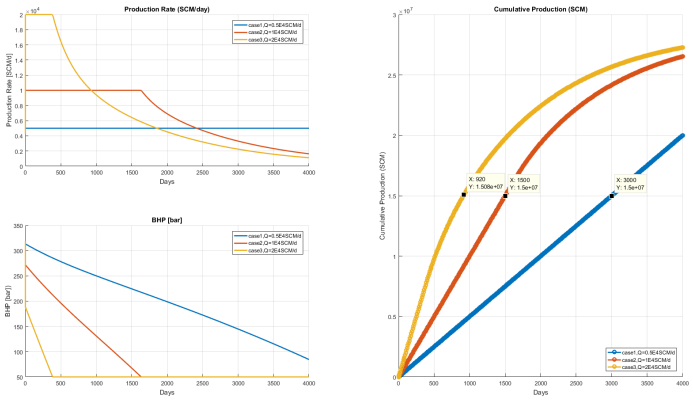

Figure B.2: Production profile; rates, BHP and cumulative production for 215 m offset fault

3. 440 m. The maximum cumulative production is around 15 million m^3. The day of simulation taken for comparing low rate, base case and high rate are 2640 day, 1510 day and 1080 day, respectively, at cumulative gas produced 13 million m^3.

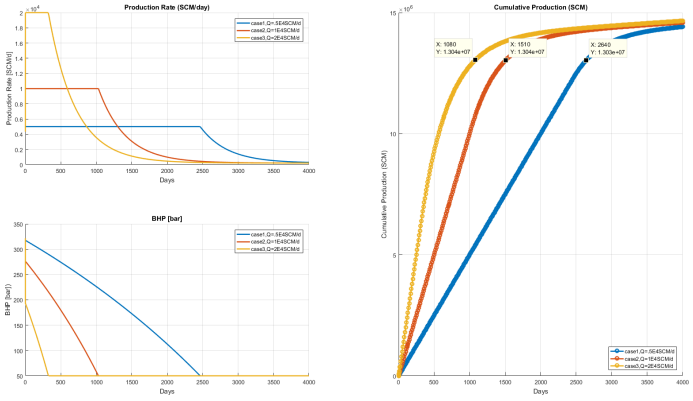

Figure B.3: Production profile; rates, BHP and cumulative production for 440 m offset fault

The variability of production rate on the production in the footwall block during depletion in the hanging wall block is studied for more variant production rate. The case was only performed for 215 m fault shift and 440 m fault shift.

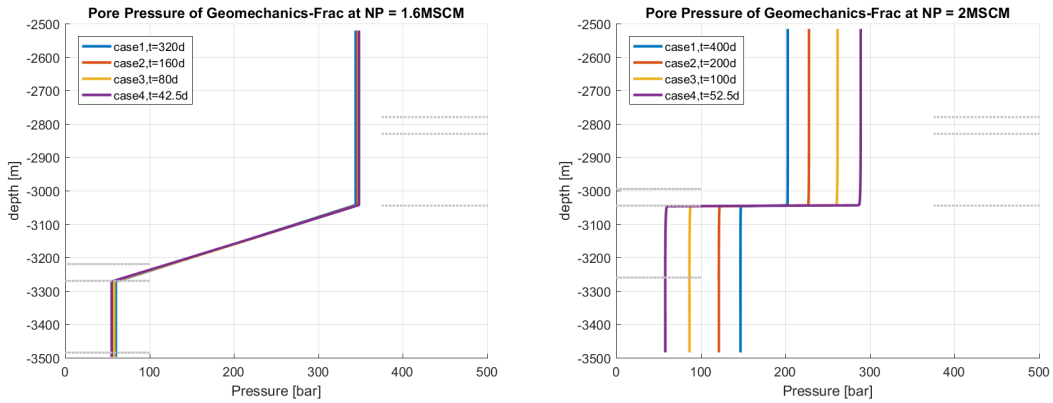

Figure B.4: Variability of production rate on different fault shift

Bibliography

[1] Nederlandse Aardolie Maatschappij. Technical Addendum to the Winningsplan Groningen 2013 - Subsidence, Induced Earthquakes and Seismic Hazard Analysis in the Groningen Field. Technical report, 2013.

[2] Birendra Jha and Ruben Juanes. Coupled multiphase flow and poromechanics: A computational model of pore pressure effects on fault slip and earthquake triggering. *Water Resources Research*, 50(5):3776–3808, may 2014.

[3] T. T. Garipov, M. Karimi-Fard, and H. A. Tchelepi. Discrete fracture model for coupled flow and geomechanics. *Computational Geosciences*, 20(1):149–160, 2016.

[4] Mark D. Zoback. *Reservoir geomechanics*. Cambridge University Press, 2007.

[5] M. Karimi-Fard, L.J. Durlofsky, and K. Aziz. An Efficient Discrete-Fracture Model Applicable for General-Purpose Reservoir Simulators. *SPE Journal*, 9(02):227–236, jun 2004.

[6] Ruslan Rin, Pavel Tomin, Timur Garipov, Denis Voskov, and Hamdi Tchelepi. General Implicit Coupling Framework for Multi-Physics Problems. *SPE International*, (SPE 182714-MS), 2017.

[7] P.A.J. van den Bogert, Jan Van Elk, and Dirk Doornhof. Impact of various modelling options on the onset of fault slip and the fault slip response using 2 - dimensional Finite - Element modelling. 2015.

[8] Loes Buijze, Peter A.J. Van Den Bogert, Brecht B.T. Wassing, Bogdan Orlic, and Johan Ten Veen. Fault reactivation mechanisms and dynamic rupture modelling of depletion-induced seismic events in a Rotliegend gas reservoir. *Geologie en Mijnbouw/Netherlands Journal of Geosciences*, 96(5):s131–s148, 2017.

[9] Jonny Rutqvist, Antonio P Rinaldi, Frédéric Cappa, and George J Moridis. Modeling of fault reactivation and induced seismicity during hydraulic fracturing of shale-gas reservoirs. *Journal of Petroleum Science and Engineering*, 107:31–44, 2013.

[10] Frédéric Cappa and Jonny Rutqvist. Modeling of coupled deformation and permeability evolution during fault reactivation induced by deep underground injection of CO2. *International Journal of Greenhouse Gas Control*, 5(2):336–346, mar 2011.

[11] Christopher J. Spiers, Suzanne J.T. Hangx, and André R. Niemeijer. New approaches in experimental research on rock and fault behaviour in the Groningen gas field. *Geologie en Mijnbouw/Netherlands Journal of Geosciences*, 96(5):s55–s69, 2017.

[12] Tom Postma and Jan Dirk Jansen. The Small Effect of Poroelastic Pressure Transients on Triggering of Production-Induced Earthquakes in the Groningen Natural Gas Field. *Journal of Geophysical Research: Solid Earth*, 123(1):401–417, 2018.

[13] Nicola Castelletto. Thermoporoelastic Modelling of Deep Aquifer Injection and pumping by mixed finite elelemts and finite volumes. *Elements*, page 138, 2010.

[14] V. I. Osipov. Physicochemical theory of effective stress in soils. *Physicochemical Theory of Effective Stress in Soils*, pages 1–55, 2015.

[15] Maurice A. Biot. General Theory of Three-Dimensional Consolidation. *Journal of Applied Physics*, 12(2):155–164, feb 1941.

[16] James R. Rice and Michael P. Cleary. Some basic stress diffusion solutions for fluid-saturated elastic porous media with compressible constituents. *Reviews of Geophysics*, 14(2):227, 1976.

[17] T. T. Garipov, K.A. Levonyan, M. Karimi-Fard, and H.A. Tchelepi. Coupled Geomechanics and Flow in Fractured Porous Media. sep 2012.

[18] Denis V Voskov and Hamdi A Tchelepi. Comparison of nonlinear formulations for two-phase multi-component eos based simulation. *Journal of Petroleum Science and Engineering*, 82:101–111, 2012.

[19] Donald Gautier. Carboniferous-Rotliegend Total Petroleum System Description and Assessment Results Summary. *U.S. Geological Survey*, Bulletin 2:1–28, 2003.

[20] Nederlandse Aardolie Maatschappij. Groningen Pressure Maintenance (GPM) Study - Progress Report February 2016. 2016.

[21] K. van Thienen-Visser and J. N. Breunese. Induced seismicity of the Groningen gas field: History and recent developments. *The Leading Edge*, 34(6):664–671, 2015.

[22] Christophe Geuzaine and Jean-François Remacle. Gmsh: A 3-D finite element mesh generator with built-in pre- and post-processing facilities. *International Journal for Numerical Methods in Engineering*, 79(11):1309–1331, sep 2009.

[23] Utkarsh Ayachit, Berk Geveci, Cory Quammen, Dave Demarle, Ken Moreland, Andy Bauer, Ben Boeckel, Dan Lipsa, Mathieu Westphal, Joachim Pouderoux, Shawn Waldon, Aashish Choudhary, Sujin Philip, George Zagaris, Burlen Loring, Thomas Maxwell, John Patchett, James Ahrens, Boonthanome Nouanesengsy, and Bill Sherman. The ParaView Guide. page 251, 2016.

[24] MATLAB. *version 9.1.0.441655 (R2016b)*. The MathWorks Inc., Natick, Massachusetts, 2016.

[25] Olivier Coussy. *Poromechanics*. 2004.

[26] L. P. Dake. *Fundamentals of reservoir engineering*. Elsevier, 1978.

[27] Christian David, Teng-Fong Wong, Wenlu Zhu, and Jiaxiang Zhang. Laboratory measurement of compaction-induced permeability change in porous rocks: Implications for the generation and maintenance of pore pressure excess in the crust. *Pure and Applied Geophysics PAGEOPH*, 143(1-3):425–456, 1994.

[28] T.T. Garipov, M. Karimi-Fard, and H.A. Tchelepi. Fully coupled flow and geomechanics model for fractured porous media. *48th US Rock Mechanics/Geomechanics Symposium*, 14(7460), 2014.

[29] J. Byerlee. Friction of rocks. *Pure and Applied Geophysics PAGEOPH*, 116(4-5):615–626, 1978.

[30] F M M Mulder. *Modelling of stress development and fault slip in and around a producing gas reservoir*, volume PhD. 2003.

[31] The finite element method for solid and structural mechanics. In O.C. Zienkiewicz, , R.L. Taylor, , and David Fox, editors, *The Finite Element Method for Solid and Structural Mechanics (Seventh Edition)*. Butterworth-Heinemann, Oxford, seventh edition edition, 2014.

[32] N. Barton, S. Bandis, and K. Bakhtar. Strength, deformation and conductivity coupling of rock joints. *International Journal of Rock Mechanics and Mining Sciences & Geomechanics Abstracts*, 22(3):121–140, jun 1985.

[33] J.C. Simo and T.A. Laursen. An augmented lagrangian treatment of contact problems involving friction. *Computers & Structures*, 42(1):97–116, jan 1992.

[34] Dominik Zbinden, Antonio Pio Rinaldi, Luca Urpi, and Stefan Wiemer. On the physics-based processes behind production-induced seismicity in natural gas fields. *Journal of Geophysical Research: Solid Earth*, 122(5):3792–3812, 2017.